

The Albedo Pattern of Mimas at Far-Ultraviolet Wavelengths

Amanda R. Hendrix¹, Timothy A. Cassidy², Bonnie J. Buratti¹, Chris Paranicas³,
Candice J. Hansen⁴, Ben Teolis⁵, Elias Roussos⁶, E. Todd Bradley⁷, Peter Kollmann⁶,
Robert E. Johnson⁸

¹ Jet Propulsion Laboratory, California Institute of Technology

Mail Stop 230-205

Pasadena, CA 91109

² Laboratory for Atmospheric and Space Physics, University of Colorado

392 UCB

Boulder, CO 80309

³ Applied Physics Laboratory, Johns Hopkins University

Laurel, MD 20723

⁴ Planetary Science Institute

Tucson, AZ 85719

⁵ Southwest Research Institute

San Antonio, TX 78238

⁶Max Planck Institute for Solar System Research
37191 Katlenburg-Lindau, Germany

⁷University of Central Florida
Orlando, FL 32816

⁸University of Virginia
Charlottesville, VA 22904

Manuscript pages: 26

Figures: 12

Tables: 1

Proposed Running Head: Mimas' FUV Albedo Pattern

Please send editorial comments to:

Amanda R. Hendrix

Jet Propulsion Laboratory, California Institute of Technology

Mail Stop 230-205

Phone 818.393.1628

Fax 818.393.4669

arh@jpl.nasa.gov

Abstract.

We present Cassini Ultraviolet Imaging Spectrograph (UVIS) observations of Mimas at far-ultraviolet wavelengths (170-190 nm) which show an interesting albedo variation centered on the anti-Saturnian hemisphere. We discuss the photometric behavior of Mimas in the far-UV and review the important exogenic processes and their expected effects, relevant over a wide range of wavelengths. We suggest that the UVIS images display the brightening effects of E-ring grain accretion on Mimas' trailing hemisphere; we also show VIMS results that are consistent with E-ring grain accretion on the trailing hemisphere. The UVIS results also suggest the production of hydrogen peroxide by photolysis in the southern hemisphere.

Keywords: satellites, composition; ices, UV spectroscopy; Saturn, satellites;
ultraviolet observations; Satellites, surfaces

1.0 Introduction.

Mimas is the innermost of Saturn's classical medium-sized moons. It is 397 km in diameter and orbits at 3.08 Saturn radii (R_S). Voyager images of Mimas revealed an old, heavily cratered surface, dominated by the large Herschel crater near the leading hemisphere equator (Smith et al. 1981). Its surface composition, based on visible-near-infrared (VNIR) data, is dominated by H_2O ice (Cruikshank et al. 1998; Cruikshank et al. 2005). It has a high visible albedo ($p \sim 1.0$, Verbiscer et al. 2007) and a flat spectrum in the visible (Buratti 1984) consistent with H_2O ice.

Using Voyager data, Buratti et al. (1990) found that Mimas may be somewhat brighter and redder (based on the red/violet ratio) on the trailing hemisphere than on the leading hemisphere; this was attributed to E-ring particle accretion. Enceladus and its south polar plume are the source of the broad E-ring (Porco et al. 2006), within which Mimas orbits. Dynamical modeling of the E-ring grains (Hamilton and Burns, 1994) showed that, due to the orbital eccentricities of the grains, those at the orbit of Mimas (inside the $3.95 R_S$ orbit of Enceladus) overtake Mimas in its orbit and are expected to bombard or coat the trailing hemisphere, while at Tethys and the other satellites exterior to Enceladus, the E-ring grains impact primarily the satellite leading hemispheres.

Using Cassini Imaging Subsystem (ISS) images, Schenk et al. (2011) found in a similar ratio (IR/UV) that the leading hemisphere is dominated by a lens-shaped feature that is blue-ish (i.e., relatively bright at 340 nm). The leading hemisphere lens appears to correlate with a region of anomalously high thermal inertia (Howett et al. 2011) measured by Cassini Composite Infrared Spectrometer (CIRS) and may

be related to energy deposited into the ice by high-energy electrons that move in a retrograde motion with respect to Mimas (Schenk et al. 2011; Paranicas et al. 2011).

Prior to Cassini, Mimas had not been studied deep in the UV. (The Voyager UV filter was centered on 350 nm.) The ultraviolet is an important wavelength regime for studying the effects of space weathering processes, because primarily the uppermost layers of the regolith and grains are sensed. Here we present far-ultraviolet (FUV) results from observations of Mimas by the Cassini Ultraviolet Imaging Spectrograph (UVIS). The results are compared with visible wavelength images from Cassini ISS and thermal data from Cassini CIRS.

2.0 Data Sets and Analysis.

The Cassini UVIS (Esposito et al. 2004) uses two-dimensional CODACON detectors to provide simultaneous spectral and one-dimensional spatial images; the second spatial dimension is acquired by slewing the UVIS slit across the target body. The far-UV channel of UVIS covers the 111.5-191.2 nm range. The detector format is 1024 spectral pixels by 64 spatial pixels. Each spectral pixel is 0.25 mrad and each spatial pixel is 1 mrad projected on the sky; the low-resolution slit used for the observations discussed here has a spectral resolution of 0.48 nm and spatial IFOV of 1.5 mrad in the spectral dimension. Here we discuss four observations, which took place during two Cassini orbits, described in Table I. Three of the observations were mosaics, where the UVIS slit was placed at distinct locations on the surface. The fourth observation (126MI_ICYLON003) consisted of three swaths across the body to make an image. Each of these swaths lasted approximately 26 min and the entire

observation was 80 min; the integration time was 120 sec. The observational geometry is shown in Fig. 1. In this analysis, we focus on 126MI_ICYLON003, as it provides the most complete coverage, and compare with the other three observations, which are used primarily for photometric analysis. We average the three swaths of 126MI_ICYLON003, and also examine the first swath only, when the spatial resolution was highest.

(Table 1 goes here)

(Figure 1 goes here)

We analyze the data in terms of the reflectance, which is given as $r=I/F$; I is the measured signal from Mimas and πF is the incident solar flux. The measured signal is dependent not only on the albedo of Mimas but also on the photometric properties of the surface, as discussed further in the next Section. We used solar data measured by SOLSTICE on the SORCE spacecraft (McClintock et al., 2000), scaled to Mimas' heliocentric distance on the days of the observations, with the proper time difference to get the correct solar longitude.

The FUV spectra of the icy Saturnian moons all show the strong signature of water ice, an absorption edge near 165 nm (e.g., Hendrix and Hansen 2008; Hendrix et al. 2010). As a result, the spectra of Mimas and the other moons are generally bright *longward* of 165 nm and dark *shortward* of 165 nm; in this analysis we focus on the longer-wavelength end of the H₂O absorption. In Fig. 2 we show the I/F

measured during the three swaths at wavelengths 170-190 nm. The data have been calibrated and RTG background subtracted. In these images, the data are “smoothed” in that the image accounts for smear within each pixel due to motion of the body during the observation. Figure 2 also shows a representation of Mimas at the mid-time of each observation, to display the viewing and lighting geometry. We note that, in the FUV data, there is no indication of Herschel crater, consistent with the idea that UVIS senses the uppermost layers of the surface. Since Herschel is a relatively old feature, this emphasizes that the effects discussed below are young.

(Figure 2 goes here)

3.0 Photometric correction.

We wish to remove the variations in signal that derive from photometry, in order to determine the normal albedo of Mimas’ surface. To estimate the UV photometric characteristics of Mimas, we follow the methods of Buratti et al. (e.g., Buratti and Veverka, 1983; Buratti 1984; Buratti 1985; Buratti et al., 1990). A simple form of a photometric function that has been used with many solar system surfaces is

$$I/F = Af(\alpha)\mu_0/(\mu + \mu_0) + (1-A)\mu_0 \quad (1)$$

where A represents the fraction of light that is singly scattered (dependent on the albedo) and $f(\alpha)$ represents the combined effects of mutual scattering among the

particles, macroscopic roughness and the single-particle phase function; α is the phase angle. The terms μ and μ_0 are the cosines of the emission and incidence angles, respectively. For $A=1$, all light is singly-scattered. The first term of Eq. 1 represents “lunar-like” scattering, where limb-darkening is not significant and single scattering dominates. The second term in Eq. 1 represents Lambert scattering.

(Figure 3 goes here.)

In Figure 3, we display data from scans along the photometric equator (ω) (after e.g. Buratti, 1984) for each of the four Mimas observations. The photometric equator is defined as the line intersecting the sub-solar and sub-observer points on the surface. For each of these scans, we have solved for the best-fit values of $f(\alpha)$ and A in the photometric model of Eq. 1. We find good fits to the scans for 126MI_ICYLON001 and 126MI_ICYLON002 using this model, demonstrating that the surface can be represented using a constant A value and thus relatively little albedo variation at this resolution. However, the same model applied to 126MI_ICYON003 does not provide a very close fit, and this is interpreted as being due to FUV albedo variations across the surface observed in this observation. Toward the anti-Saturnian hemisphere (positive $\sin(\omega)$ values in Fig. 3c for this observational geometry), the surface is brighter (higher albedo) than predicted, and toward the leading hemisphere (negative $\sin(\omega)$ values in Fig. 3c), the surface is darker (lower albedo) than predicted. Similarly, the model fits the ICYLON008 scan adequately

toward the trailing hemisphere (positive $\sin(\omega)$ values in Fig. 3d for this observational geometry) but the surface is brighter than predicted toward the anti-Saturnian hemisphere (negative $\sin(\omega)$ values in Fig. 3d). We use the best-fit photometric model for ICYLON003 to correct the observation for the photometric behavior of the surface and study the resultant normal albedo.

4.0 Results.

The far-UV normal albedo pattern of Mimas is shown in Fig. 4 for the ICYLON003 observation; the normal albedo was derived by dividing the measured data by the photometric correction as described in Section 3.0. An albedo variation across the surface is evident. A bright region, which appears to be centered near the apex of the anti-Saturnian hemisphere ($\sim 180^\circ\text{W}$), extends from $\sim 20^\circ\text{S}$ to the north pole, and wraps over the north pole on to the high latitudes of the leading hemisphere; the bright region is ~ 3 times brighter than the darker region. The bright region in the north is not mirrored in the southern hemisphere, on the observed anti-Saturnian region, resulting in a latitudinal asymmetry in albedo. To study this a bit further, we show (Fig. 5) scans within two latitude bands plotted against geographic longitude. Both scans show a dramatic (non-photometric) dropoff in brightness toward the leading hemisphere. The southern hemisphere scan is lower in brightness overall than the northern hemisphere scan. This is not expected to be due to photometric characteristics of the regolith, as both the sub-solar point and the sub-spacecraft point are near the equator. Thus, the overall FUV albedo pattern differs from that measured at visible wavelengths (Schenk et al. 2011) or thermal wavelengths

(Howett et al. 2011), and it does not follow the “lens” shape of the longer wavelengths; this is discussed further in the Section. 6.0

The reflectance spectra of the FUV-bright region and the FUV-dark region are shown in Fig. 6. Both spectra show the water ice absorption edge near 165 nm (e.g. Hendrix et al. 2010); because water ice is so bright longward of 165 nm, the difference between the spectra suggests that the UV-bright region is richer in water ice than the UV-dark region.

(Figure 4 goes here.)

(Figure 5 goes here.)

(Figure 6 goes here.)

5.0 Exogenic Processes at Mimas.

There are many weathering processes that act on the satellite surfaces in the Saturnian system, including bombardment by photons, charged and neutral particles, and ice grains as shown in the diagram of Fig. 7. To aid in the interpretation of the UVIS results, we discuss each of these processes and their expected results.

(Figure 7 goes here.)

5.1 E-ring grains

As mentioned previously, E-ring grains preferentially impact the trailing hemisphere of Mimas (Hamilton and Burns, 1994). The exact accretion pattern of these grains is not completely known, but their speeds are different enough that we expect a broad bombardment distribution onto the surface of Mimas. The solution for their orbits depends on factors such as their initial rate of speed, charging history, etc. Since simulations of E-ring grain orbital inclinations (Horanyi et al. 2008) show that they can grow quite large (e.g., 15°), the latitudinal extent (vertical profile) of the E ring is much greater than Mimas' radius. Therefore, we expect that there are grain trajectories that at least reach the polar regions of Mimas. A schematic diagram of the estimated pattern of E-ring grain accretion on Mimas is shown in Fig. 8a.

(Figure 8 goes here.)

5.2 Cold plasma

An additional exogenic process on the trailing hemisphere is bombardment by the corotating cold plasma. The expected bombardment pattern is a “bulls-eye” shape on the trailing hemisphere but we cannot comment extensively on any potential UV effects based on the lack of trailing hemisphere coverage in the UVIS dataset to date. However, the central part of the trailing hemisphere could be slightly darker than the high latitudes and anti-Saturnian region (Fig. 4e), possibly an effect of plasma darkening of that region. Schenk et al. (2011) note a weak

IR/NUV bright region in Cassini images of the Mimas trailing hemisphere, which was suggested could be due to cold plasma bombardment. The expected pattern of bombardment of cold plasma is shown in Fig. 8b. We also expect any nanograins to bombard the trailing hemisphere in a similar manner.

5.3 High-energy electrons

In contrast to the plasma and low-energy (below ~ 1 MeV) electrons discussed above, electrons with energies above ~ 1 MeV, because of their retrograde drifts in the dipole field of Saturn, preferentially bombard the leading hemisphere of Mimas (Schenk et al. 2011; Paranicas et al. 2011). This interaction results in the “lens” feature seen in ISS data (Schenk et al. 2011) as well as the thermal anomaly seen in CIRS data (Howett et al. 2011). The electron intensity strongly depends on energy. Going from 1 to 10 MeV, the intensity drops by approximately four orders of magnitude (Fig. 9; Kollman et al. 2011). Most of the energy is therefore deposited by ~ 1 MeV electrons in Mimas’ surface.

(Figure 9 goes here.)

We also note that there is enhanced darkening in the Saturnward and anti-Saturnward portions of Mimas’ leading hemisphere lens (Schenk et al. 2011). A direct comparison between the ISS ratio image and a UVIS image is shown in Fig. 10, where the ISS ratio image (Fig. 10a) is projected at same perspective and resolution as the UVIS image of Fig. 4a. The dark “ansa” of the lens is obvious in the ISS data at

this resolution (though the albedo contrast is quite low compared to the UVIS image); the surface here is relatively bright at 340 nm. Thus, the ISS ratio image displays a distinct variation in IR/UV3 brightness across the lens (at the level of ~10%), with the ansae being brightest. The UVIS image (Fig. 10b) hints at an “ansa” in the bright region near 150°W (this only appears in the ICYLON003 swath 1 image of Fig. 4a and Fig. 10b; it is not so apparent in the ICYLON003 averaged image, Fig. 4b); however, whereas the ISS ratio, hence the NUV albedo stays relatively constant in value between ~90-140°W, the UVIS albedo grows darker with decreasing longitude in this region.

(Figure 10 goes here.)

This enhanced darkening in the ISS IR/UV ratio at the ansae of the lens may be explained if we take into consideration additional components of energetic electron drifts near the moon. These components occur due to the electromagnetic field perturbations that should exist downstream of Mimas.

The main interaction mode in Mimas’s interaction with the magnetosphere is thought to be plasma absorption, as earlier studies indicate that Mimas cannot sustain a substantial sputter-produced atmosphere that may lead to a Europa or Io-type of magnetospheric interaction (Saur and Strobel, 2005). Plasma absorbing moons have their interaction region downstream with respect to the cold plasma corotation flow. The main feature of this interaction region is a plasma cavity (or wake) that forms due to absorption at the moon’s trailing hemisphere. Plasma is

almost absent in the deep wake and refills within few moon radii downstream (Roussos et al., 2008).

The presence of this cold plasma wake gives rise to a series of disturbances in the electric and magnetic fields. For instance, the requirement for the total pressure to remain approximately constant (magnetic plus plasma pressure), leads to an increase of the magnetic field intensity in the wake center, since plasma pressure has been lost there (diamagnetic effect). In addition, on the two sides of the central wake, the magnetic field decreases, so that $\nabla B=0$ is satisfied in the system (Khurana et al. 2008).

These deviations from the undisturbed magnetic field increase toward the moon and result in magnetic field gradients in the nominal corotation direction. These field gradients lead to radially inward or outward drifts, as shown in Figure 11. Importantly the center of the wake loses electrons to the gradient drift, and positions such as the leading hemisphere apex do not receive the full flux of the retrograde drifting electrons. These electrons will tend to follow contours of $\delta B \sim 0$ that are at the edges of the plasma wake, as shown, so that there is preferential bombardment of the sub- and anti-Saturnian portions of the leading hemisphere. These locations are situated where the Mimas lens feature is darker in the ISS ratio image (Schenk et al. 2011 and Fig. 10a). The expected pattern of bombardment by high-energy electrons, including the enhanced bombardment at the lens ansae, is shown in Fig. 8c.

(Figure 11 goes here.)

A simple pressure balance calculation, using for instance parameters from Saur and Strobel (2005), indicates a field enhancement in the wake between 0.3 and 0.5 nT, in a background field of about 740 nT. While such an increase is small (and so are the associated field gradients), radial gradient drifts will be enforced due to the energy of the electrons involved. MeV electrons are strongly magnetized, meaning that their drift will be dominated by magnetic field gradients, not electric fields (e.g. the corotation or other wake-associated electric fields) (Paranicas et al., 2009).

The electrons impacting Mimas are removed from the magnetosphere. This causes a corridor of small electron intensities around Mimas (and the other icy moons). The corridor is continuously refilled so that a steady state forms. Mimas is exposed to the electrons within the corridor (no matter where they came from) and is not exposed to the electrons outside the corridor.

6.0 Interpretation of UVIS results considering the exogenic processes & effects.

6.1 Spectral effects of E-ring grain accretion

The FUV spectral variation between the UV-dark region of the central leading hemisphere and the UV-bright region of the anti-Saturnian hemisphere (Figs. 4 and 6) suggests more water ice in the UV-bright region. This is consistent with the idea of E-ring grains accreting on the surface in the bright region, which would be expected to deliver relatively pure water ice to the surface. The albedo variation

suggests that E-ring grains reach high latitudes (at least in the north – the latitudinal asymmetry is discussed below). The interaction between the fine E-ring grains and the surface is expected to be dominant on the trailing hemisphere (Hamilton and Burns, 1994; Buratti et al. 1998), consistent with the westward brightening in ICYLON003 and the brighter trailing hemisphere in ICYLON008 (Fig. 4).

One additional method of understanding the accretion of Saturn's E-ring grains onto Mimas is to look for changes in particle sizes on its surface as measured by the Cassini Visual Infrared Mapping Spectrometer (VIMS). VIMS is an imaging spectrometer with 352 spectral channels between the wavelengths of 0.30 to 5.1 μm (Brown et al., 2004). The spectral region between 1 and 2.5 μm is particularly rich in the characteristic absorption bands of volatiles and minerals and is thus well-suited to identifying and mapping the composition of surfaces. In addition, the positions of the spectral bands of water ice near 1.05, 1.3, 1.52 and 2.0 μm are known to change as the particle size changes (Clark and Lucey, 1984). Because the E-ring is dominated by particles in the 0.1-1.0 μm size range (Kempf et al., 2008), an abundance of small particles would be consistent with an enhanced flux from the E-ring as discussed below.

(Figure 12 goes here.)

The left side of Fig. 12 shows VIMS spectra extracted from three regions on Mimas: the northern rim of the large crater Herschel; the center of the leading side, and the center of the trailing side (each spectrum is averaged from 20 pixels). A

band depth was calculated for the two deepest spectral lines, at 1.52 μm and 2.0 μm , by the following formula

$$(R_C - R_B) / R_C$$

where R_C is the relative reflectance of the continuum and R_B is the relative reflectance at the center of the band position. The continuum was computed by fitting a straight line to it and computing the value of that line at the center of the band position. The right side of Fig. 12 shows these results for both bands plotted with the predictions of Clark and Lucey (1984). The band depths on the trailing side (10-50 μm) are substantially less than those on the leading side (20-80 μm) and imply smaller particles on average. Hershel has the largest grain sizes of any region of Mimas (50-100 μm). These results are consistent with a flux of smaller particles from the E-ring impacting the trailing hemisphere of Mimas.

The derived grain sizes of the surface of Mimas are substantially greater than the sizes of particles in the E-ring. Thus, there must be a process (perhaps annealing) that acts subsequently to the accretion of the particles, causing regolith grain growth.

6.2 Chemical effects: H_2O_2 production

We suggest that the UVIS images are also showing compositional variations across the surface that are due to radiation- and photolysis-induced chemistry. In particular, hydrogen peroxide (H_2O_2) is readily produced both by radiolysis and

photolysis of ice (e.g., Johnson and Quickenden 1997; Cooper et al. 2003). Peroxide is known to absorb efficiently in the UV, even in small amounts (e.g., Carlson et al. 1999) and is thought to cause reddening in the UV on other icy satellites (e.g., Hendrix et al. 1999; Hendrix and Johnson 2008). Using the high-energy electron distribution at Mimas (Paranicas et al. 2011) with a lower bound of 1 MeV together with laboratory measurements (e.g. Gerakines et al. 1996, Hand and Carlson 2011, Teolis et al. 2009 and references therein), we find that the concentration of H_2O_2 in ice from radiolysis only is $1.1\text{e-}3\%$; for UV photons only, the concentration is 1.9% . Considering that electrons also contribute to the destruction of H_2O_2 , we estimate that the concentration of H_2O_2 in ice from radiolysis and photolysis is $0.64\text{e-}2\%$. Considering that Carlson et al. (1999) show a strong absorption (a factor of >4 decrease in reflectance between 330 nm and 210 nm) with just 0.13% H_2O_2 in ice, it is plausible that hydrogen peroxide is causing the FUV-darkness on the leading-southern region of Mimas. The measurement was made ~ 6 months after equinox; we anticipate that UVIS is sensing peroxide created in the surface ice of Mimas by the combination of photons and electrons throughout the ~ 7 year southern summer timeframe. Figure 8d shows a representation of the estimated distribution of photolytically-produced peroxide for the observation timeframe.

Figures 8e and 8f show a model of the combined estimated effects of the exogenic processes discussed here. The model reproduces the large-scale FUV albedo variations seen on Mimas. The model was produced by layering the component models in Figs. 8a-8d and assuming that E-ring grain accretion (brightening) dominates on the trailing hemisphere and wraps around onto the

leading hemisphere; but on the southern portion of both the leading and trailing hemispheres the photolytic production of H_2O_2 (darkening) dominates. We estimate that photolysis produces H_2O_2 globally, but that this is particularly pronounced in the southern regions for this timeframe. On the trailing hemisphere, the darkening of H_2O_2 is offset by the brightening effect of E-ring accretion; on the trailing hemisphere it is expected that cold plasma contributes to radiation darkening of the surface but we do not include this component in our combination model because that effect is not seen from the perspective of the UVIS observation considered here. We also do not include the possible effects of high-energy electrons as we expect that these particles (mostly) penetrate too deeply to be sensed by UVIS. Rates of H_2O_2 production compared with E-ring grain accretion need to be studied further, along with rate of annealing which likely contributes to the destruction of the fine E-ring grains (i.e., grain growth). We note that, even in the “bright” regions on Mimas, the albedo is lower than the expected albedo of pure water ice (Hendrix et al. 2010), indicating that there is photolytic production of H_2O_2 (and/or darkening by cold plasma bombardment) in this region at Mimas subsequent to the accretion of the E-ring grains, and/or the E-ring grains are not pure H_2O ice (perhaps some processing has occurred en route to Mimas).

6.3 Sampling and penetration depths

The fact that UVIS measures the leading hemisphere low latitudes of Mimas to be relatively dark is interesting, because this is also the area where ISS measurements show the surface to be relatively bright in the near-UV (340 nm) – the blue “lens” (Schenk et al. 2011) previously mentioned. This lens is relatively bright in the NUV

(340 nm); the UVIS results, in the far-UV, suggest that the low latitudes of the leading hemisphere are relatively dark (along with the southern latitudes). We consider the idea that the UVIS, ISS and CIRS measurements are sensing different depths in the surface layer. Mimas and the other icy Saturnian satellites exhibit a dramatic absorption at near-UV wavelengths ($\sim 200\text{-}350$ nm); they are very dark at FUV wavelengths (Hendrix et al., 2010) while being bright in visible. There is thus a significant albedo change between the ISS UV filters and the UVIS data sets. This absorption is important in understanding the difference in albedo patterns. Estimating the wavelength-dependent optical constants for Mimas' surface, the absorption path length near 180 nm is on the order of a few microns, while it is on the order of centimeters at 340 nm. Paranicas et al. (2009) demonstrate that high-energy electrons or the secondary photons emitted as they slow down can deposit energy to a depth of about 1 m (1 MeV electrons have a penetration depth of 0.4 cm); thus the electrons produce damage and effects at deeper levels in the regolith than are sensed by UVIS. The uppermost layers of the regolith are dosed on both hemispheres, but the leading hemisphere will also have the deeper penetration. Therefore, the CIRS-measured thermal anomaly exhibits a spatial morphology different from the UVIS-measured albedo. That is, CIRS is sensing the effect of the deeply-penetrating high-energy electrons while UVIS senses primarily the effects in the very top-most layers modified by the $\sim 1\text{-}\mu\text{m}$ E-ring grains and H_2O_2 production. The ISS images display effects at intermediate depths. Thus the model of Fig. 8e applies to the shallow sensing depths of FUV wavelengths only. At these FUV

wavelengths, the high-energy electrons are not as important as E-ring grains and photolysis, the effects of which will overlay the mostly deeper electron effects.

7.0 Conclusions.

Mimas has a surprisingly interesting far-UV (170-190 nm) albedo pattern, as measured by Cassini UVIS, and appears to be the result of a combination of processes. The anti-Saturnian hemisphere and north polar region are brighter than the leading hemisphere; this extends somewhat onto the trailing hemisphere though observations there are of lower resolution. This brightening is consistent with E-ring grain accretion which is also demonstrated in the VIMS dataset. On the trailing hemisphere a competing process is plasma bombardment which tends to darken the surface by enhancing absorption at these wavelengths; this competition may explain why the trailing hemisphere is not overwhelmingly brighter than the leading hemisphere; in fact the primary FUV bright region may actually be the anti-Saturnian region discussed here and also likely on the not-observed sub-Saturnian region - regions where the E-ring grain accretion occurs and the plasma bombardment is minimal (confined to a bulls-eye pattern on the trailing hemisphere).

We anticipate that photolysis produces H_2O_2 globally, but that this is particularly pronounced in the southern regions for this timeframe. We note that, even in the “bright” regions on Mimas, the albedo is lower than the expected albedo of pure water ice (Hendrix et al. 2010), indicating that there is photolytic production of H_2O_2 (and/or darkening by cold plasma bombardment) in this region at Mimas subsequent to the accretion of the E-ring grains, and/or the E-ring grains are not

pure H₂O ice (perhaps some processing has occurred en route to Mimas). Rates of H₂O₂ production compared with E-ring grain accretion need to be studied further, along with rate of annealing.

The latitudinal asymmetry in the UV albedo is proposed to be the result of accumulated H₂O₂ in the surface ice over the southern summer. We expect that Mimas observations later in the Cassini mission could reveal a darkening of the northern leading hemisphere as summer approaches that region and photolysis acts to produce H₂O₂ there, while the southern hemisphere darkening is gradually erased by plating out of fresh E-ring grains.

The lens-shaped feature that appears in the ISS ratio image (Schenk et al. 2011) and the CIRS image (Howett et al. 2011) is not obvious in the UVIS images; this is attributed to the different sampling depths in the instruments and the penetration depths by the different processes. The Mimas lens does not have a uniform ratio/color value across it: the ansae are distinctly darker (i.e., brighter at 340 nm), attributed to preferential bombardment of the sub- and anti-Saturnian portions of the leading hemisphere by energetic electrons. A hint of the dark ansa on the anti-Saturnian side is seen in the UVIS data – the region is relatively dark at 170-190 nm.

The combined FUV effects detected on Mimas are probes of radiolytic and photolytic weathering processes in the Saturn system and are expected to be present to varying degrees on the other icy Saturnian moons; they will be investigated further in future studies.

Acknowledgements.

The research described in this paper was carried out at the Jet Propulsion Laboratory, California Institute of Technology, under a contract with the National Aeronautics and Space Administration. Thanks to Alain Jouchoux and the UVIS operations team at LASP for making these observations happen. We are grateful to John Spencer, Matt Hedman, Joe Burns, Michael Kokorowski, Josh Colwell, Bob West and Greg Holsclaw for helpful suggestions and ideas, and to Marty Snow for providing solar spectra.

References.

- Brown, R.H., and 21 coauthors 2004. The Cassini Visual and Infrared Mapping Spectrometer (VIMS) Investigation. *Space Sci. Rev.* **115**, 111-168.
- Buratti, B. and J. Veverka 1983. Voyager Photometry of Europa. *Icarus* **55**, 93-110.
- Buratti, B. J. 1984. Voyager Disk Resolved Photometry of the Saturnian Satellites. *Icarus* **59**, 392-405.
- Buratti, B. J. 1985. Application of a Radiative Transfer Model to Bright Icy Satellites. *Icarus* **61**: 208-217.
- Buratti, B. J., J. A. Mosher, T. V. Johnson 1990 Albedo and Color Maps of the Saturnian Satellites. *Icarus* **87**, 339-357
- Buratti, B. J., J. A. Mosher, P. D. Nicholson, C. A. McGhee, R. G. French 1998. Near -IR photometry of the Saturnian satellites during ring plane crossing. *Icarus*, Volume **136**, Issue 2, pp. 223-231
- Carlson, R. W. and 13 co-authors 1999. Hydrogen peroxide on the surface of Europa. *Science* **283**: 2062-2064.

- Clark, R. N., P. Lucey 1984. Spectral properties of ice-particulate mixtures and implications for remote sensing. I. Intimate mixtures. *J. Geophys. Res.* **89**, 6341-6348
- Cooper, P. D., R. E. Johnson, T. I. Quickenden 2003. Hydrogen peroxide dimmers and the production of O₂ in icy satellite surfaces. *Icarus* **166**: 444-446.
- Cruikshank, D. P., Brown, R. H., Calvin, W. M., Roush, T. L., Bartholomew, M. J. 1998. Ices on the Satellites of Jupiter, Saturn, and Uranus. In *Solar System Ices*, Vol. 227 579.
- Cruikshank, D.P., Owen, T.C., Dalle Ore, C., Geballe, T.R., Roush, T.L., de Bergh, C., Sandford, S.A., Poulet, F., Benedix, G.K., Emery, J.P., 2005. A spectroscopic study of the surfaces of Saturn's large satellites: H₂O ice, tholins, and minor constituents. *Icarus* 175, 268–283.
- Esposito, L.W., and 18 colleagues, 2004. The Cassini Ultraviolet Imaging Spectrograph investigation. *Space Sci. Rev.* 115, 299–361.
- Gerakines, P. A., W. A. Schutte, P Ehrenfreund 1996. Ultraviolet processing of interstellar ice analogs I. Pure ices. *Astron. & Astrophys.* **312**: 289-305.

- Hamilton, D.P., Burns, J.A., 1994. Origin of Saturn's E ring: Self-sustained, naturally. *Science* 267, 550–553.
- Hand, K. P. and R. W. Carlson 2011. H₂O₂ production by high-energy electrons on icy satellites as a function of surface temperature and electron flux. *Icarus*, *in press*.
- Hendrix, A. R. and C. J. Hansen 2008. The Albedo Dichotomy of Iapetus Measured at UV Wavelengths. *Icarus* 193: 344-351.
- Hendrix, A. R., C. J. Hansen, G. M. Holsclaw 2010. The Ultraviolet Reflectance of Enceladus: Implications for Surface Composition. *Icarus* 206: 608-617, 2010.
- Hendrix, A. R., Barth, C. A., Stewart, A. I. F., Hord, C. W., & Lane, A. L. 1999. Hydrogen peroxide on the icy Galilean satellites. *LPSC XXX*, 2043
- Hendrix, A. R., R. E. Johnson 2008. Callisto: New insights from Galileo disk-resolved UV measurements. *Astrophys. J.* **687**: 706-713.
- Horanyi, M., A. Juhasz, and G. E. Morfill 2008. Large-scale structure of Saturn's E-ring. *Geophysical Research Letters* 35, 4203-
- Howett, C. J. A. et al., A high-amplitude thermal anomaly of probably magnetospheric origin on Saturn's moon Mimas, *submitted to Icarus*, 2011.

Johnson, R. E., and T. I. Quickenden 1997. Photolysis and radiolysis of water ice on outer Solar System bodies. *J. Geophys. Res.* 102, 10,985– 10,996.

Kempf, S., U. Beckman, G. Moragas-Klostermeyer, F. Postberg, R. Srama, T. Economou, J. Schmidt, F. Spahn, E. Grün 2008. The E ring in the vicinity of Enceladus. I. Spatial distribution and properties of the ring particles. *Icarus* **193**, 420-437.

Khurana, K. K., C. T. Russell, M. K. Dougherty 2008. Magnetic portraits of Tethys and Rhea. *Icarus* **193**: 465-474.

Kollmann, P., E. Roussos, C. Paranicas, N. Krupp, C. M. Jackman, E. Kirsch, K.-H. Glassmeier 2011. Energetic particle phase space densities at Saturn: Cassini observations and interpretations. *J. Geophys. Res.*, in press.

McClintock, W.E., Rottman, G.J., Woods, T.N., 2000. Solar Stellar Irradiance Comparison Experiment II (SOLSTICE II) for the NASA Earth Observing System's Solar Radiation and Climate Experiment (SORCE) mission. *Proc. SPIE Earth Observ. Syst.* V 4135, 225–234.

Paranicas, C., J. F. Cooper, H. B. Garrett, R. E. Johnson, S. J. Sturmer 2009. Europa's radiation environment and its effects on the surface. In: Pappalardo, R. T. et al. (Eds.), Europa. Univ Arizona Press, Tucson AZ, pp. 529-544.

Paranicas, C., et al. 2011. Energetic charged particle weathering of Saturn's inner satellites, *Planet. Space Sci.*, in press.

Porco, C.C., and 24 colleagues, 2006. Cassini observes the active south pole of Enceladus. *Science* 311, 1393–1401.

Roussos, E. et al., Plasma and fields in the wake of Rhea: 3-D hybrid simulation and comparison with Cassini data, *Annales Geophysicae*, Volume 26, Issue 3, 2008, pp.619-637 (2008)

Saur, J. and Strobell, D.F., Atmospheres and Plasma Interactions at Saturn's Largest Inner Icy Satellites, *The Astrophysical Journal*, Volume 620, Issue 2, pp. L115-L118 (2005)

Schenk, P., D. P. Hamilton, R. E. Johnson, W. B. McKinnon, C. Paranicas, J. Schmidt, and M. R. Showalter 2011. Plasma, plumes and rings: Saturn system dynamics as recorded in global color patterns on its midsize satellites. *Icarus*, 211, 740-757.

Smith, B. A. and 26 co-authors 1981. Encounter with Saturn – Voyager 1 imaging science results. *Science* **212**: 163-191.

B. D. Teolis, J. Shi, R. A. Baragiola 2009. Formation, trapping, and ejection of radiolytic O₂ from ion-irradiated water ice studied by sputter depth profiling, *Journal of Chemical Physics*, Volume 130, pp. 134704.

Figure Captions.

Figure 1. Observational geometry for 126MI_ICYLON003. In this observation, the UVIS slit was oriented as shown; the slit was scanned three times across the body. The UVIS spatial pixels are indicated by the small white boxes; the green lines designate right ascension and declination.

Figure 2. Left panels: UVIS I/F images of Mimas at 170-190 nm. Right panels: Mimas representations at visible wavelengths at time of UVIS images. The leading hemisphere is centered on 90°W; the trailing hemisphere is centered on 270°W. Longitude lines are shown in 30° increments.

Figure 3. Scans along the photometric equator. The photometric equator is the line defined by the sub-solar and the sub-spacecraft points. Negative values are toward the terminator, positive values are toward the sunlit limb. Data are fit with the model of Eq. 1 (red line). Good fits are obtained especially for ICYLON001 and ICYLON002; the fit is not so good for ICYLON003 and this is interpreted as due to albedo variations across the surface. The same albedo variation may contribute to the data-model mismatch toward the terminator in ICYLON008.

Figure 4. Mimas UV (170-190 nm) normal albedo images. There is more than a factor of 3 variation in albedo across the anti-Saturnian hemisphere. The high albedo may not persist across the entire trailing hemisphere, but does not seem to

get as low as on the leading hemisphere. Longitude lines are shown in 30° increments.

Figure 5. Brightness vs. longitude in two latitude bins across Mimas (126MI_ICYLON003). The sub-solar point moved from 1.6°N, 150°W to 1.6°N, 170°W and the sub-spacecraft point moved from 7.6°S, 131°W to 3.9°S, 162°W. The sharp dropoff in brightness is not characteristic as being due to photometric properties, nor is the overall relative brightness between north and south.

Figure 6. Reflectance spectra for the UV bright and dark regions on Mimas. UVIS pixels from the indicated regions were averaged to obtain these spectra. Both regions display the water ice absorption edge near 165 nm. The “bright” region is brighter at wavelengths longer than ~165 nm, likely because of a greater abundance of fresh water ice in the uppermost layers of the surface in that region; this region is also very dark at wavelengths shorter than 165 nm and in fact the signal there is not greater than the background.

Figure 7. Diagram of exogenic processes considered to be important at Mimas. View is from above Mimas’ north pole.

Figure 8. Simplified representations to demonstrate the relative importance and contributed effects to the UV albedo from different processes. (a) Assumed E-ring grain accretion pattern. We expect that E-ring grains impact Mimas globally but that

there is a region on the leading hemisphere where lower overall abundances accumulate. Here we assume a uniform accretion by E-ring grains; we do not include any possible decrease in E-ring grain accretion away from the trailing hemisphere apex. (b) Cold plasma bombardment pattern. The plasma is expected to darken the surface but this darkening will compete with brightening by E-ring grain accretion. (c) High-energy electron bombardment pattern (after Paranicas et al. 2011), also showing the enhanced bombardment regions of the lens ansae discussed in Sec. 5.3. (d) Assumed photolysis pattern for the southern summer – equinox timeframe. (e) Model combining the different processes and assuming that the photolysis component dominates for latitudes southward of 30°S. We also do not include the high-energy electrons shown in (c) because we assume that those penetration depths are largely not seen by UVIS. The cold plasma is not included as its effects are not seen in the view as seen by UVIS. (f) Combination model shown at the same projection as the Mimas UVIS image of Fig. 4c, also shown here (g).

Figure 9. Intensity of equatorially mirroring high-energy electrons measured by MIMI/LEMMS. The error bars are 1-sigma standard deviations from the mission averaged data until February 2011. The red lines show Mimas' semi-major axis \pm its radius. The orange lines show the extent of the sweeping corridor. Its width is dominantly determined by Mimas' eccentricity and it is smeared out due to radial diffusion. The intensity within the corridor is an upper limit since there might be a contribution from background radiation.

Figure 10. (a) ISS ratio image (Schenk et al. 2010) shown at UVIS resolution and from the same perspective as the UVIS data in Fig. 1. This is the IR/UV3 ratio, so darker (green) is where the surface is relatively bright at 340 nm. (b) UVIS 126MI_ICYLON003 swath 1 image of I/F at 170-190 nm from Fig 4c.. Longitude lines are shown in 30° increments.

Figure 11. (a) Magnetic field gradients and associated radial drifts in the wake of a plasma absorbing moon at Saturn (like Mimas). The view is for the equatorial plane of the interaction region, as viewed from the north. In the sketch cold plasma comes from the left, gets absorbed on the moon (circle). A plasma cavity forms, where $\Delta B > 0$ (Region 1). Radial drifts there are antiplanetward. In Regions 2, $\Delta B < 0$ and drifts are planetward. Energetic electrons drift from the right and encounter this interaction region before impacting the moon. As drifts tend to be along $\Delta B = 0$, the MeV electrons will preferentially hit the two sides of Mimas along the planet-moon line, and avoid locations in the wake center.

(b) Curves of $\Delta B = 0$ for the plasma absorbing interaction of Rhea, based on simulation results of Roussos et al. (2008). In this plot, +x points towards corotation and +y towards Saturn, while the color indicates the magnetic field intensity, with red/blue corresponding to high/low values respectively. Access of high energy electrons at regions where $\Delta B = 0$ curves form closed loops is forbidden. Since one such region is located in the wake center, more electron flux would be deposited at the moon apices. The picture should be similar for Mimas, although deformation of

$\Delta B=0$ curves (which should be parallel lines to the x-axis in an undisturbed dipole field) should be less intense, since the $\Delta B/B$ at Mimas's wake is much smaller than at Rhea's wake.

Figure 12. (Left) VIMS spectra from three regions of Mimas: the center of both the leading and trailing hemispheres, and the crater Herschel. The wavelength is shown in microns. No evidence for any component other than water ice, including CO_2 , which has been discovered on the other medium sized satellites (Buratti et al., 2005, Clark et al., 2008), is seen. There is an as-yet unidentified spectral band near $1.8 \mu\text{m}$. (Right) The band depths of the water ice absorption band are plotted with the model of Clark and Lucey (1984). The smallest grain sizes are concentrated on the trailing side, while the larger particles are in the rim of Herschel.

Table I.

date	observation name	average Cassini altitude	sub-spacecraft longitude	phase angle	Sun-Saturn distance (AU)
2005 August 2	012MI_ICYLON008	61,407	234°W	54.6°	9.08
2010 February 13	126MI_ICYLON001	17,090	91°W	43.8°	9.49
2010 February 13	126MI_ICYLON002	32,401	120°W	25.8°	9.49
2010 February 13	126MI_ICYLON003	51,231 km	145°W	16.2°	9.49

The leading hemisphere is centered on 90°W longitude, while the anti-Saturnian hemisphere is centered on 180°W longitude.

Fig.1

[Click here to download high resolution image](#)

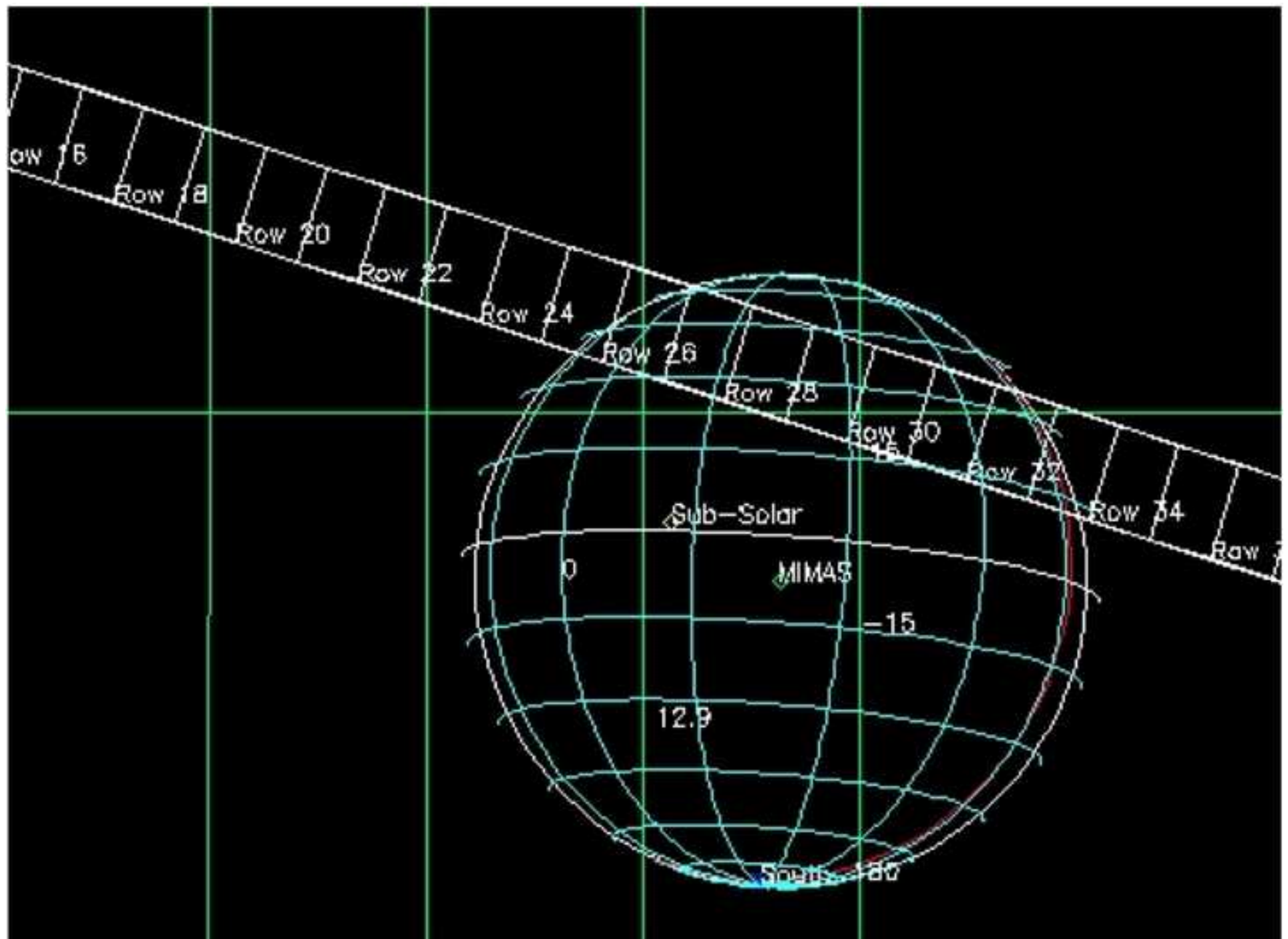


Fig.2a

[Click here to download high resolution image](#)

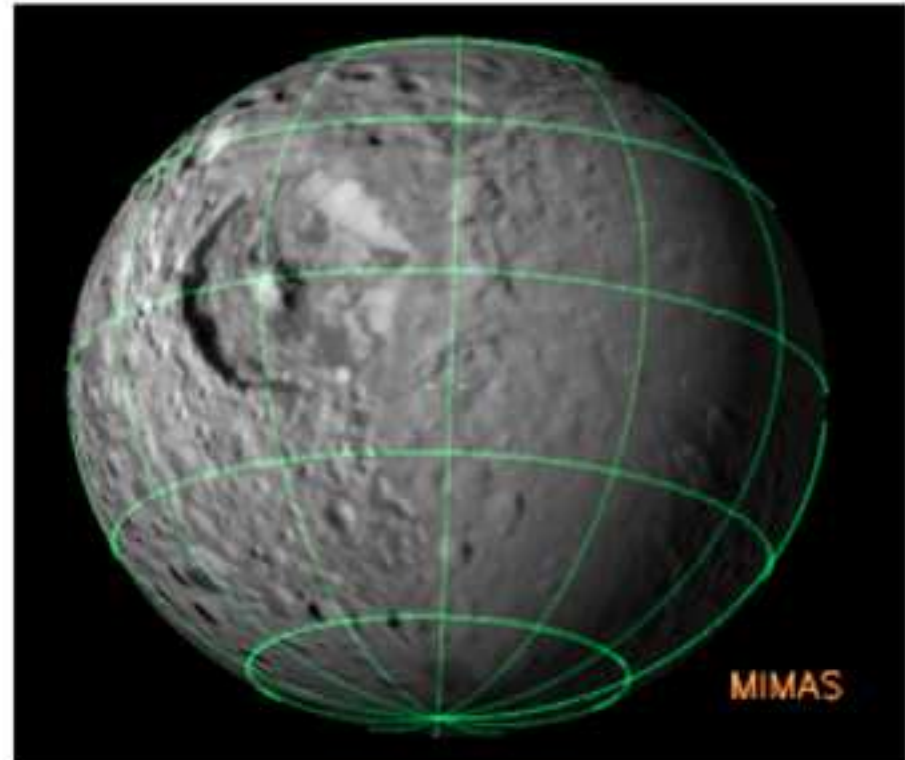
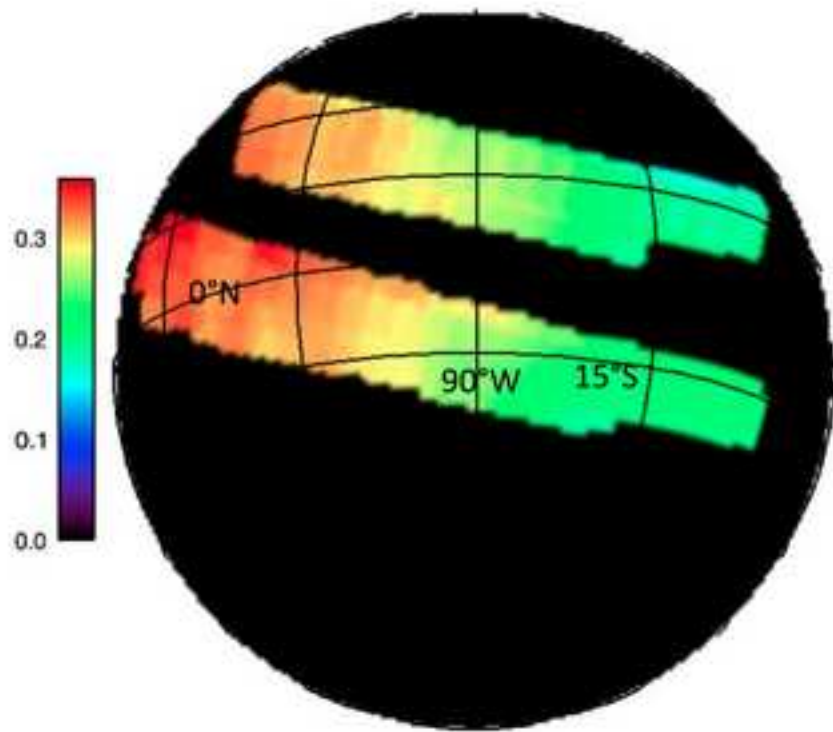


Fig.2b

[Click here to download high resolution image](#)

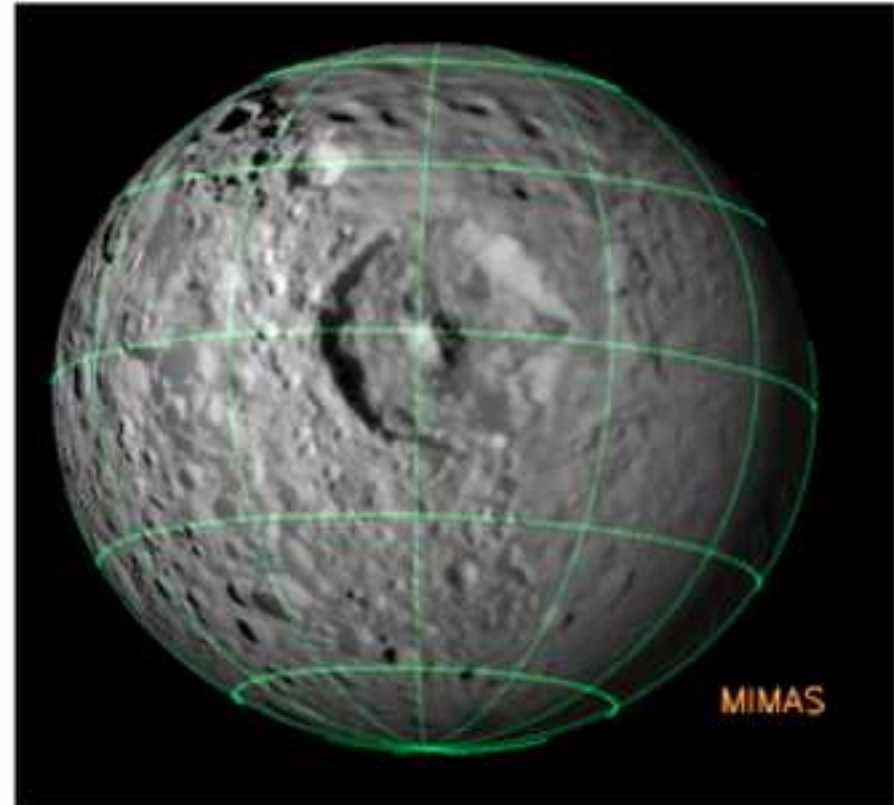
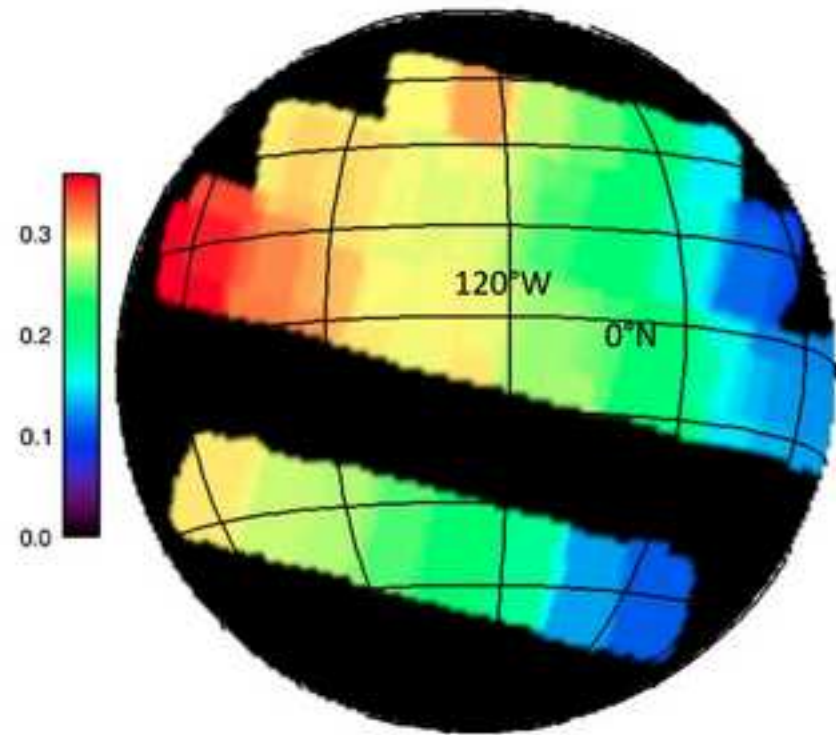


Fig.2c

[Click here to download high resolution image](#)

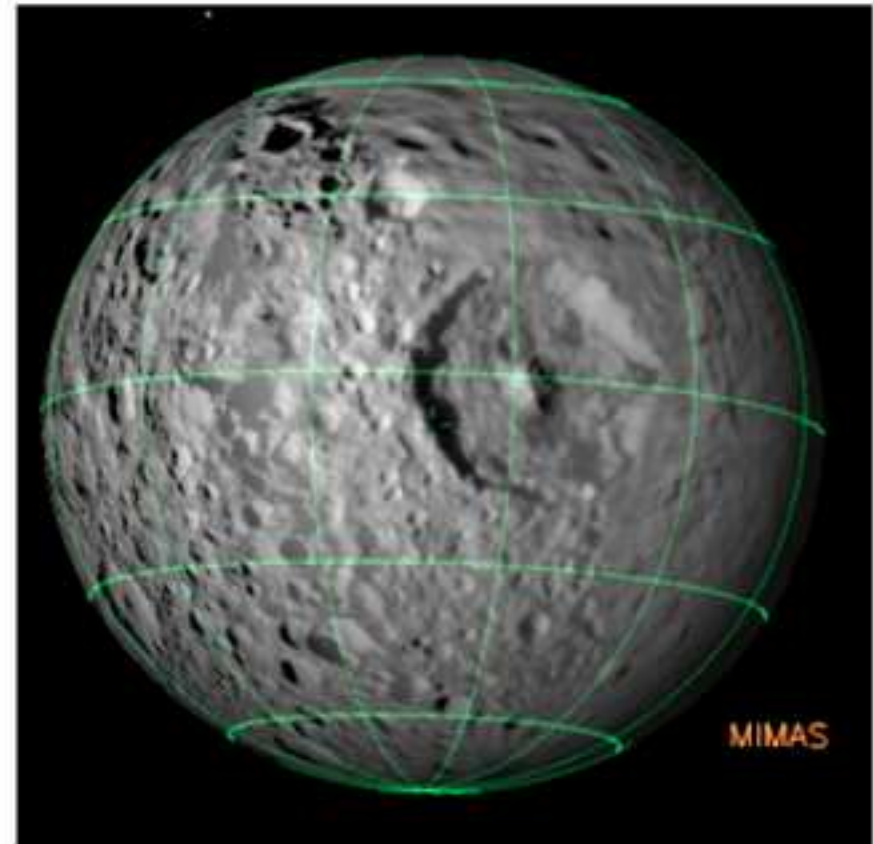
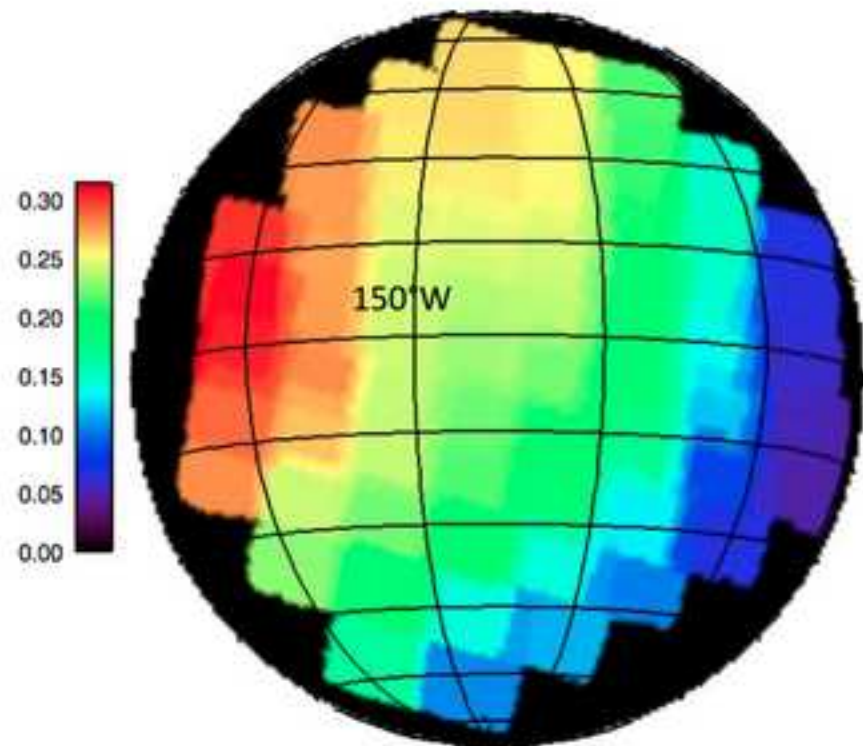


Fig.3a

[Click here to download high resolution image](#)

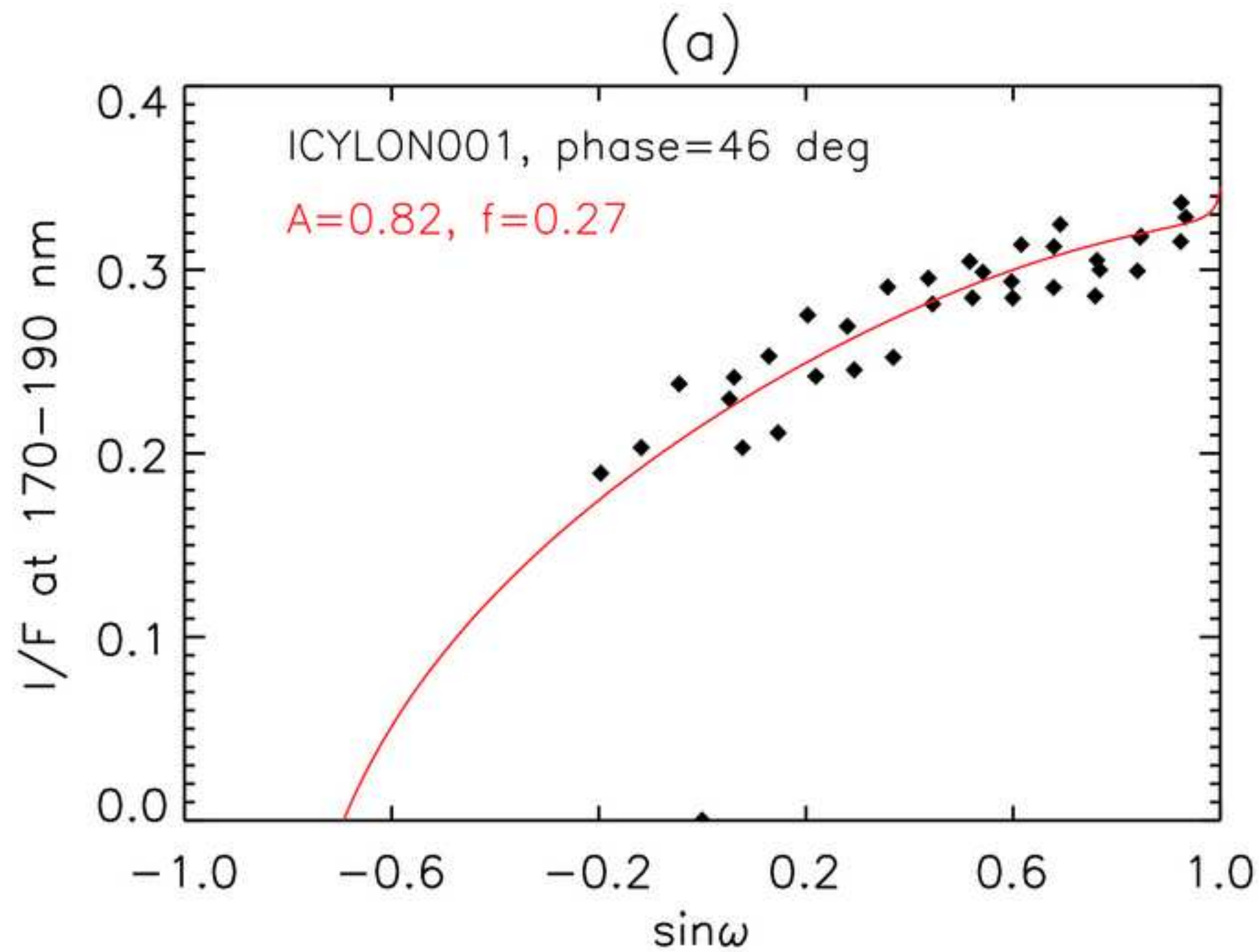


Fig.3b

[Click here to download high resolution image](#)

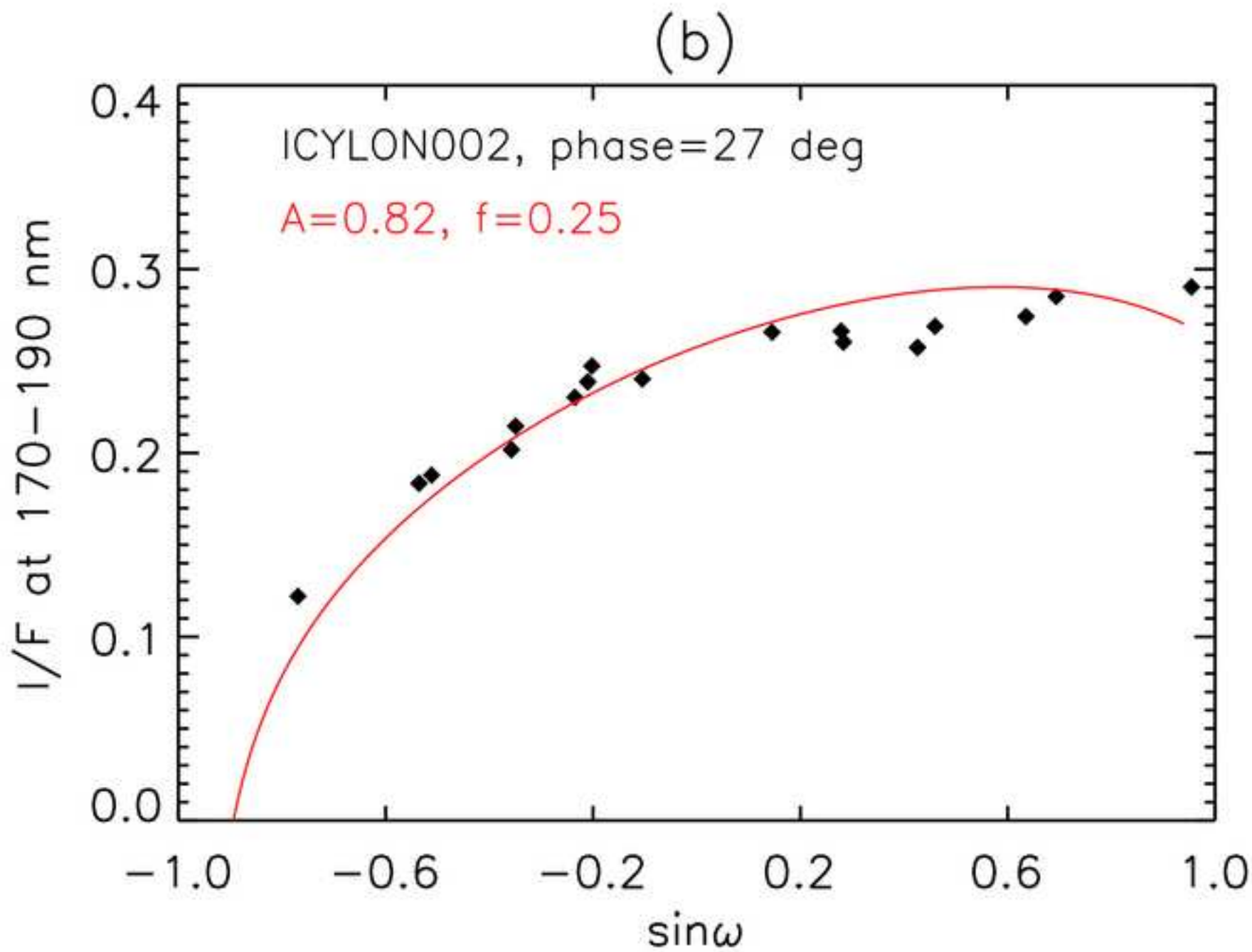


Fig.3c

[Click here to download high resolution image](#)

(c)

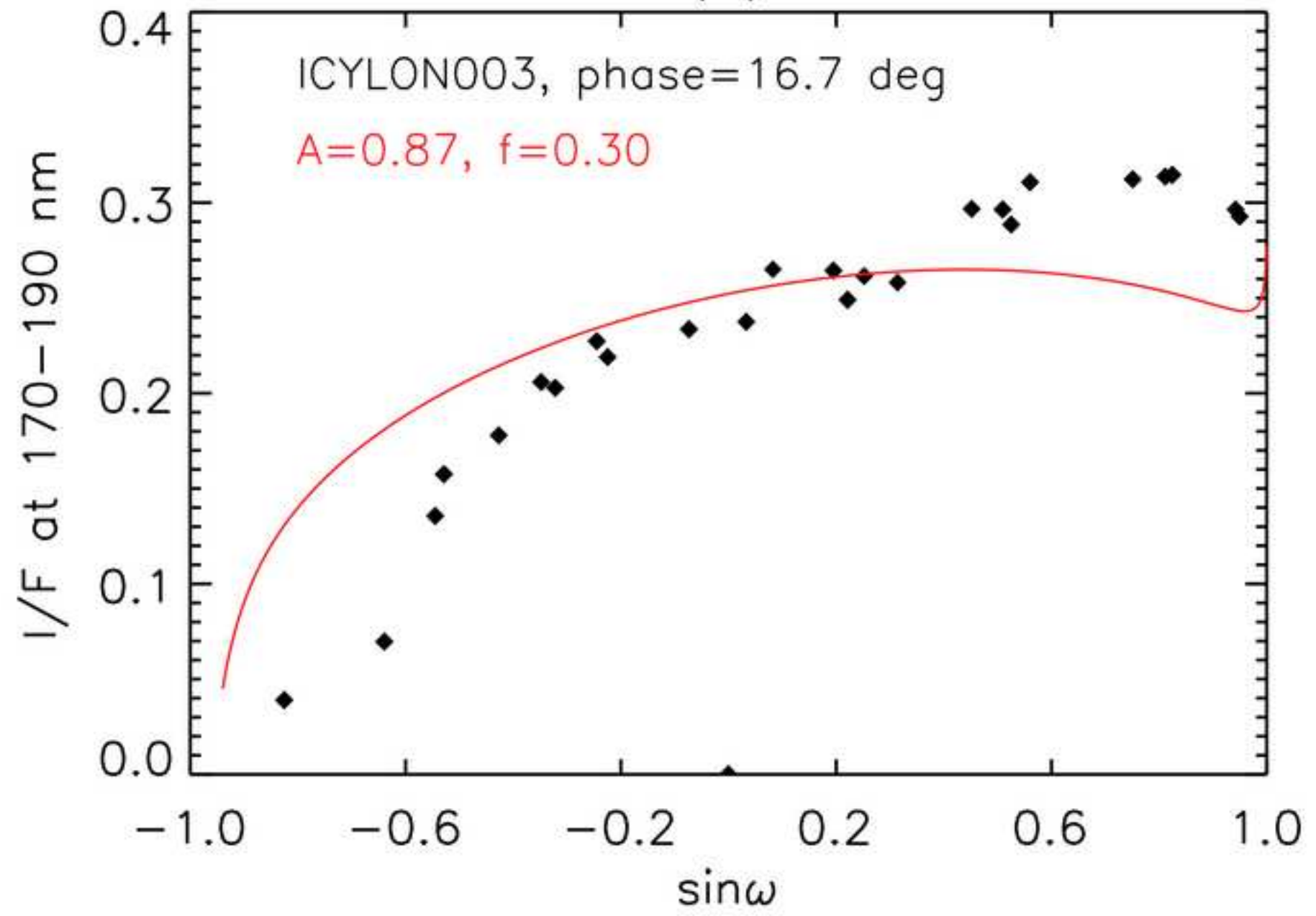


Fig.3d

[Click here to download high resolution image](#)

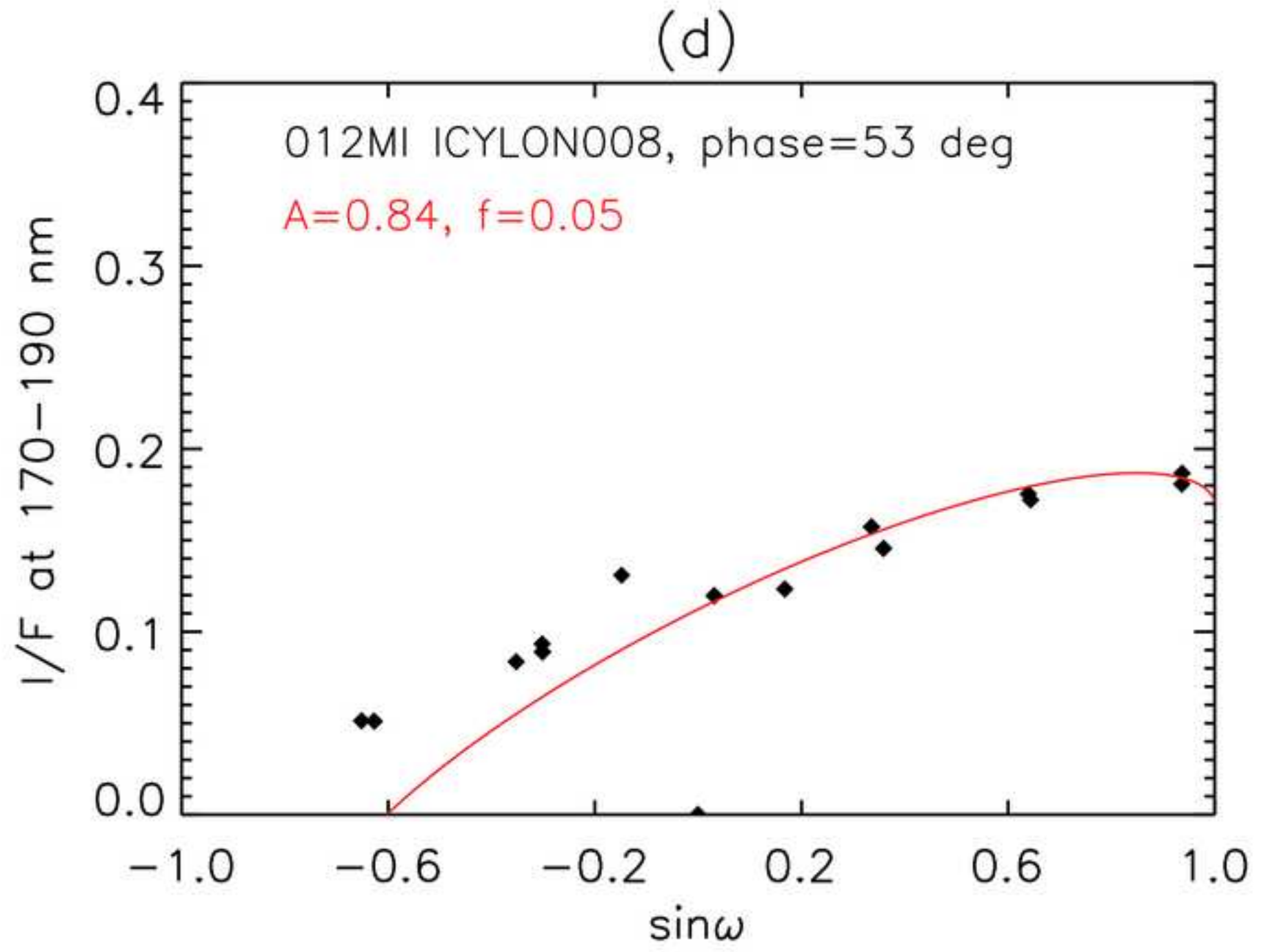


Fig.4a

[Click here to download high resolution image](#)

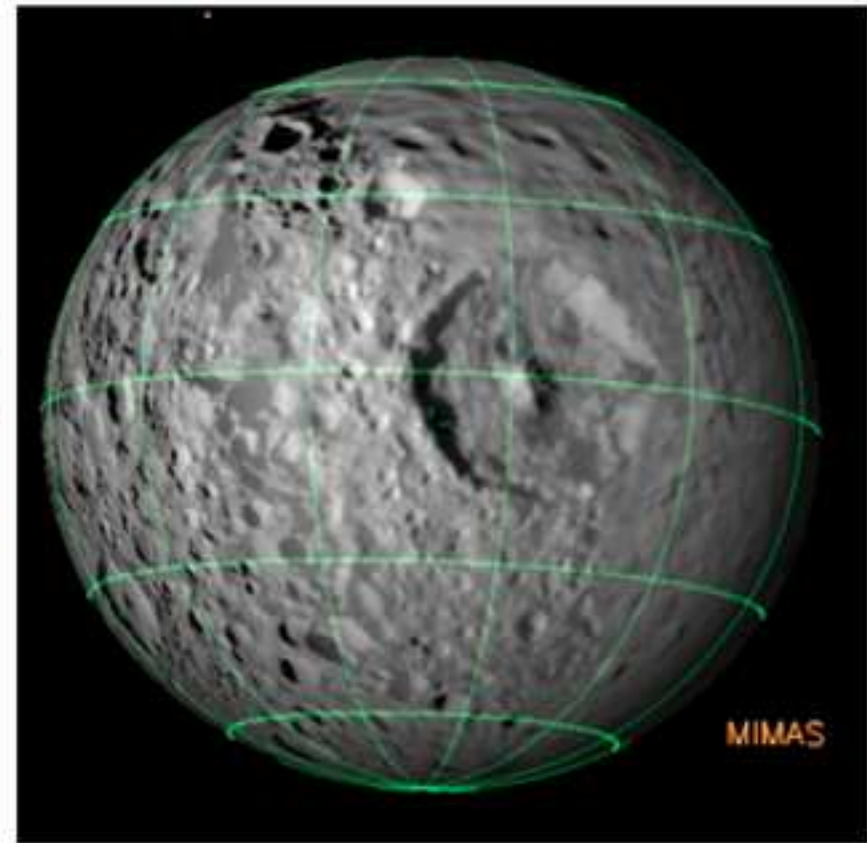
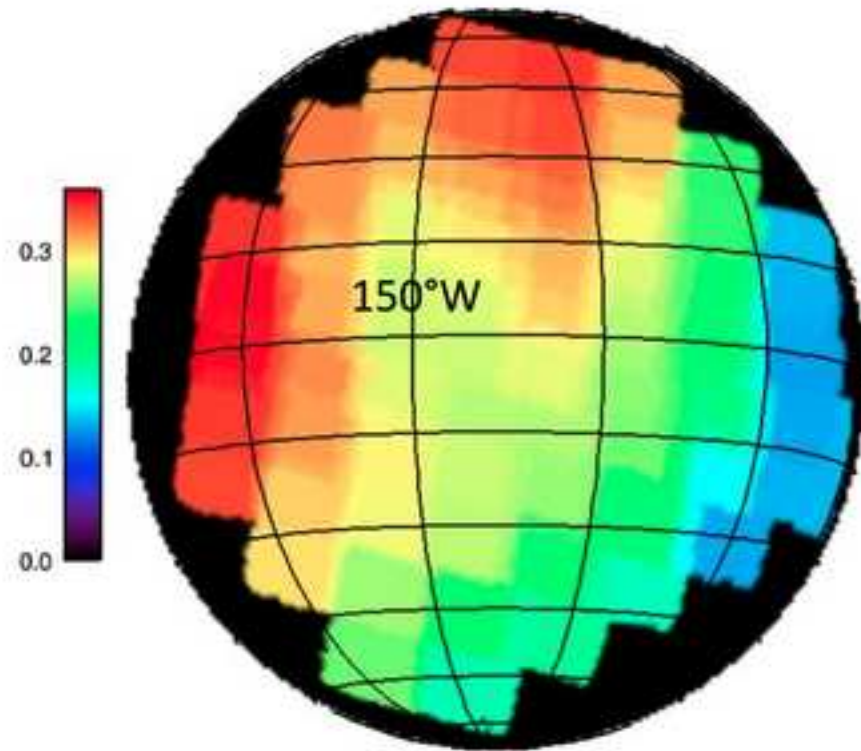


Fig. 4b
[Click here to download high resolution image](#)

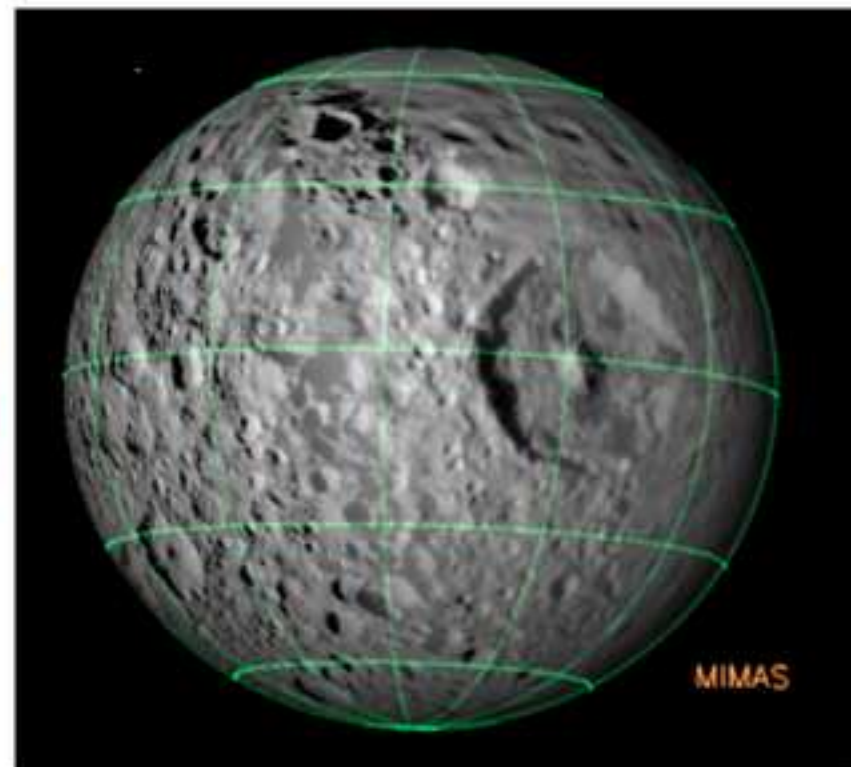
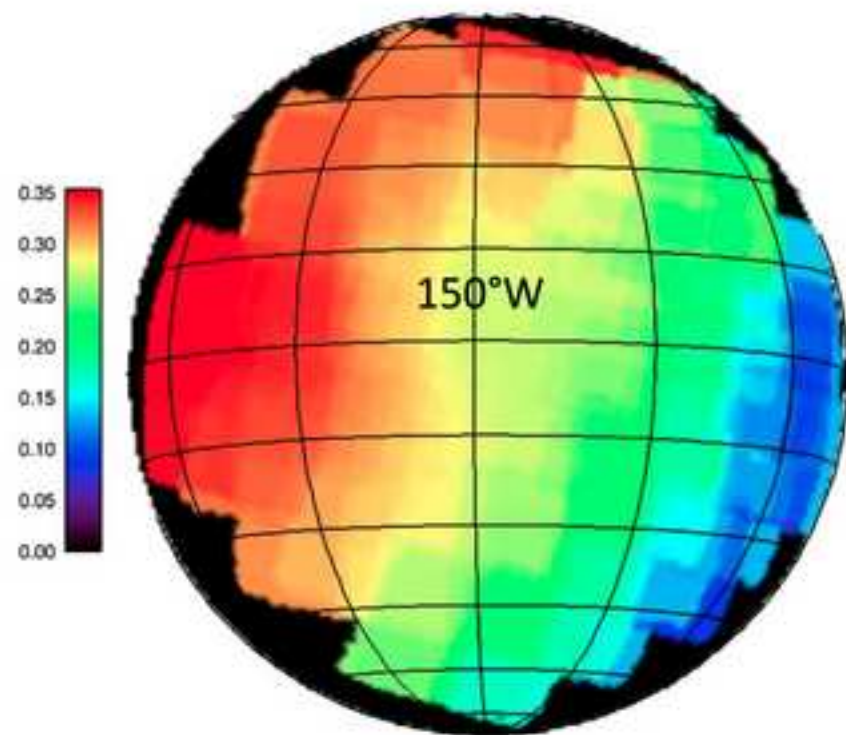


Fig. 4c
[Click here to download high resolution image](#)

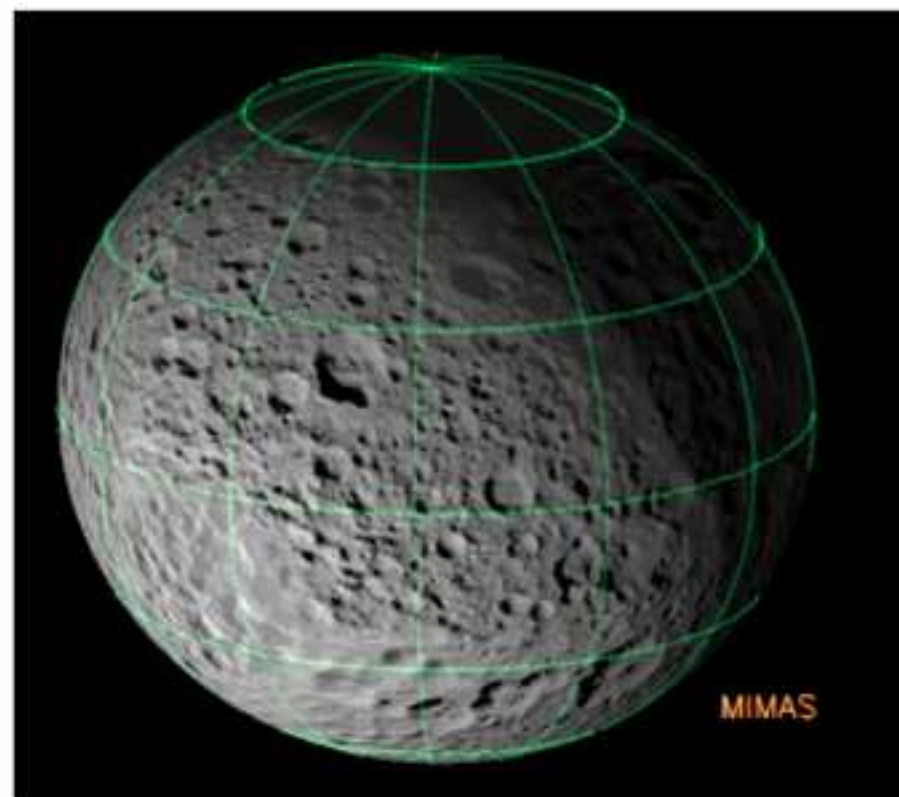
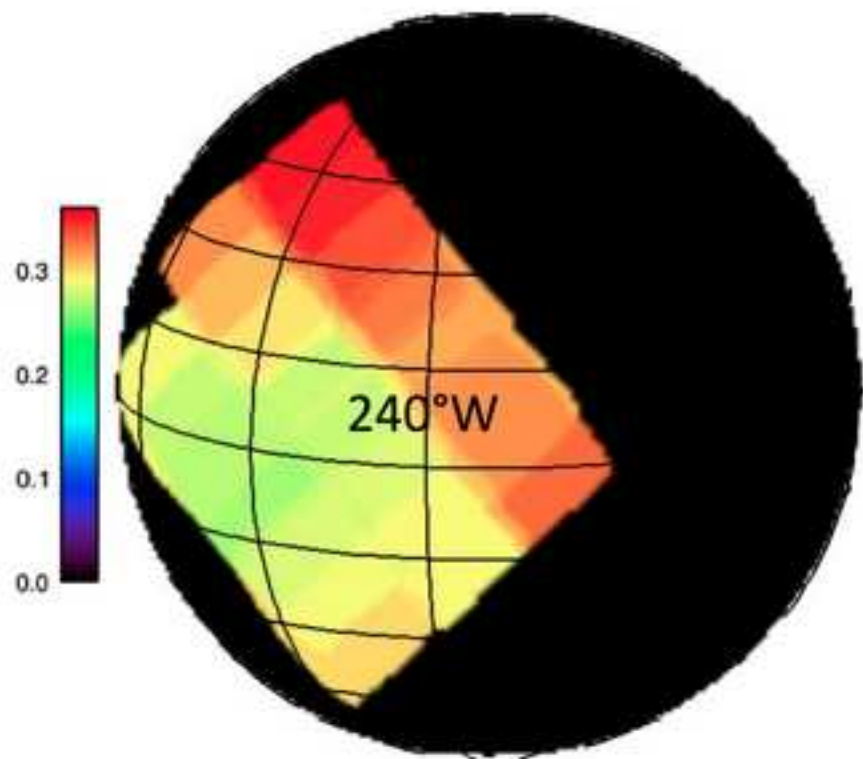


Fig. 5

[Click here to download high resolution image](#)

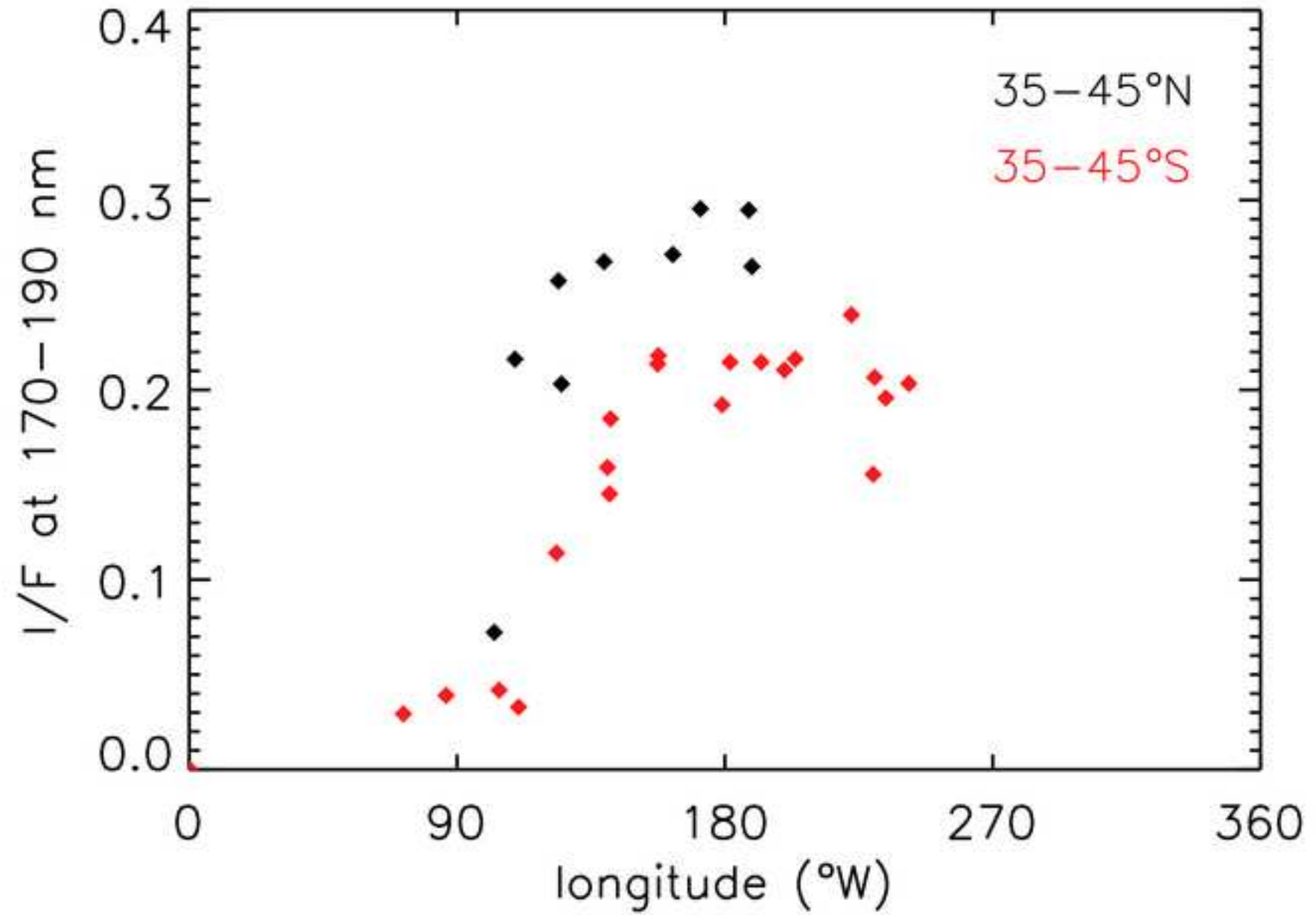


Fig. 6

[Click here to download high resolution image](#)

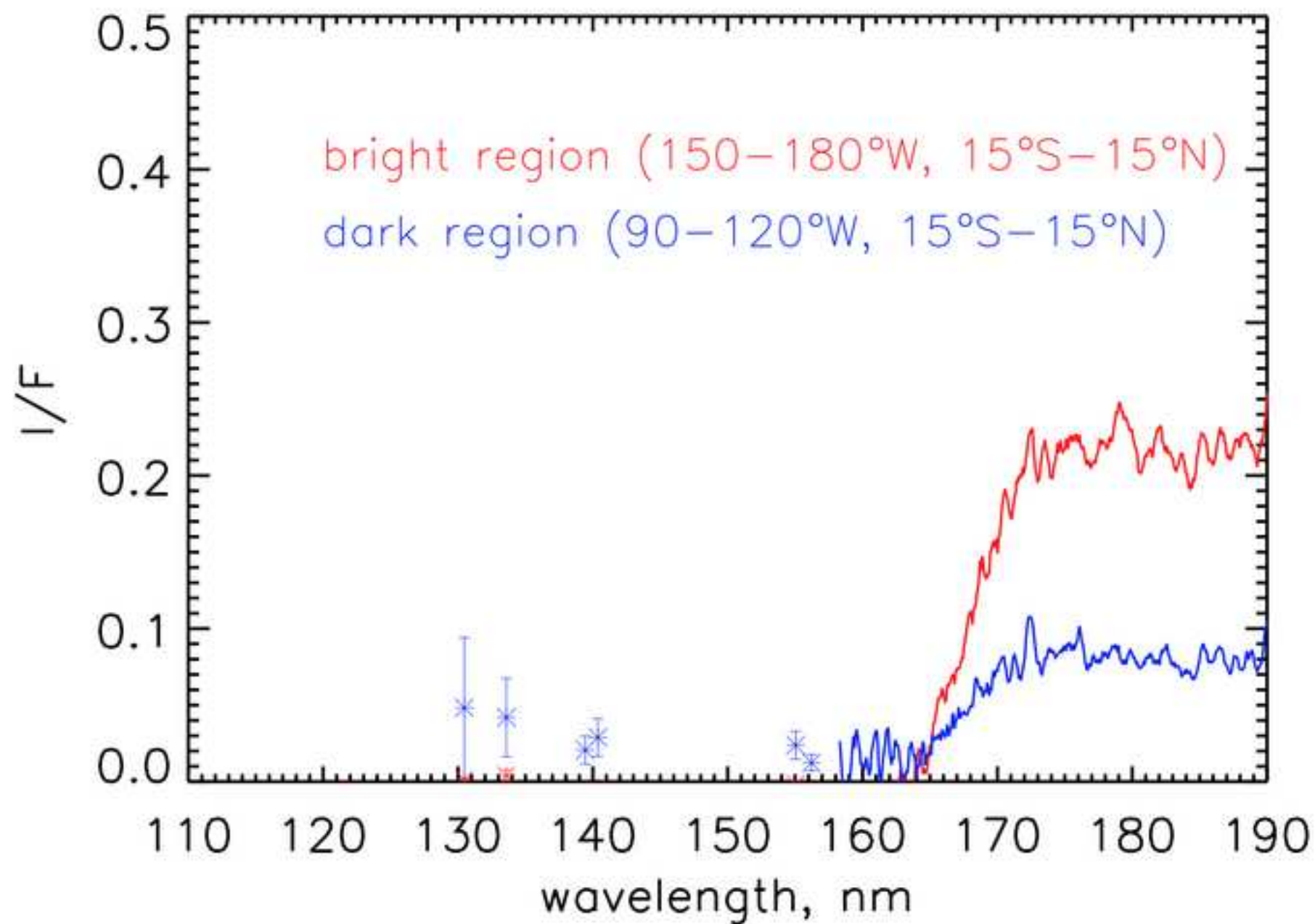


Fig. 7

[Click here to download high resolution image](#)

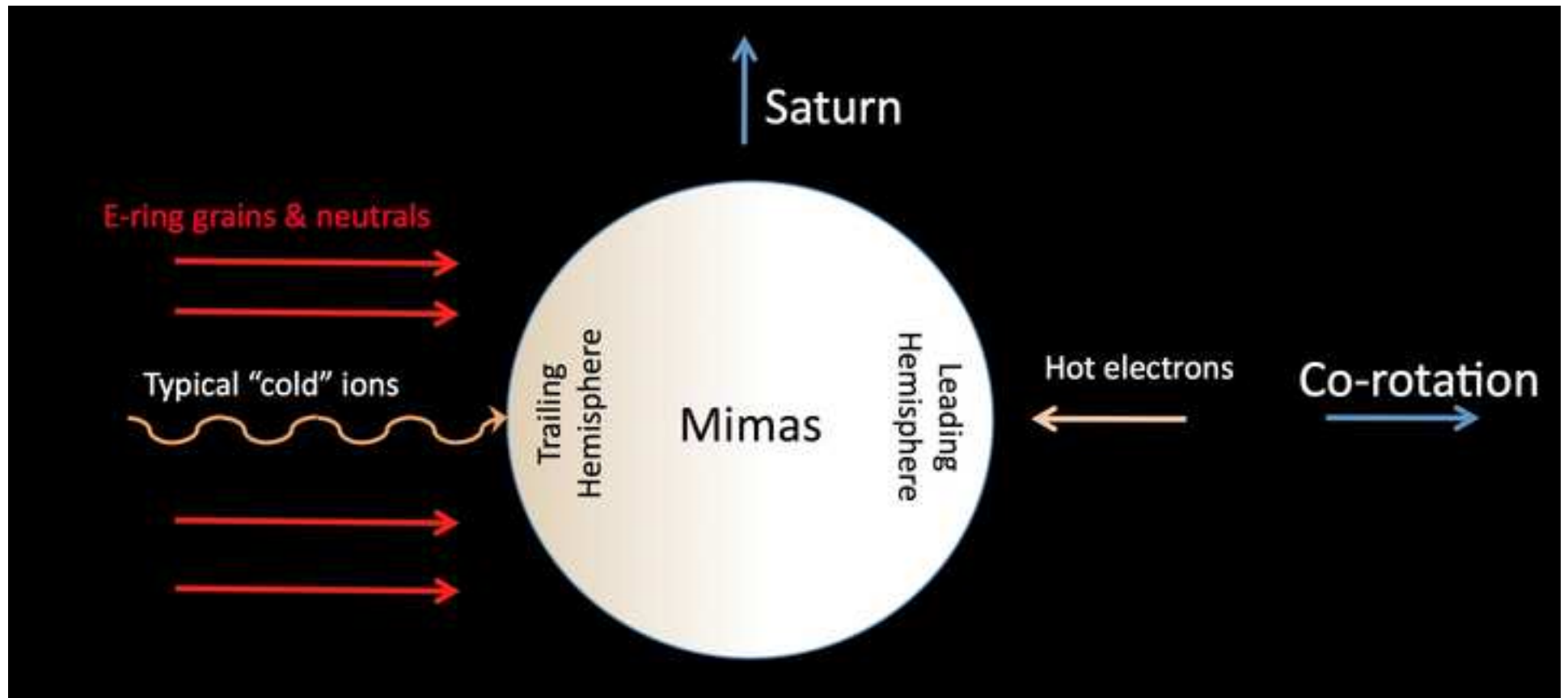


Fig. 8a
[Click here to download high resolution image](#)

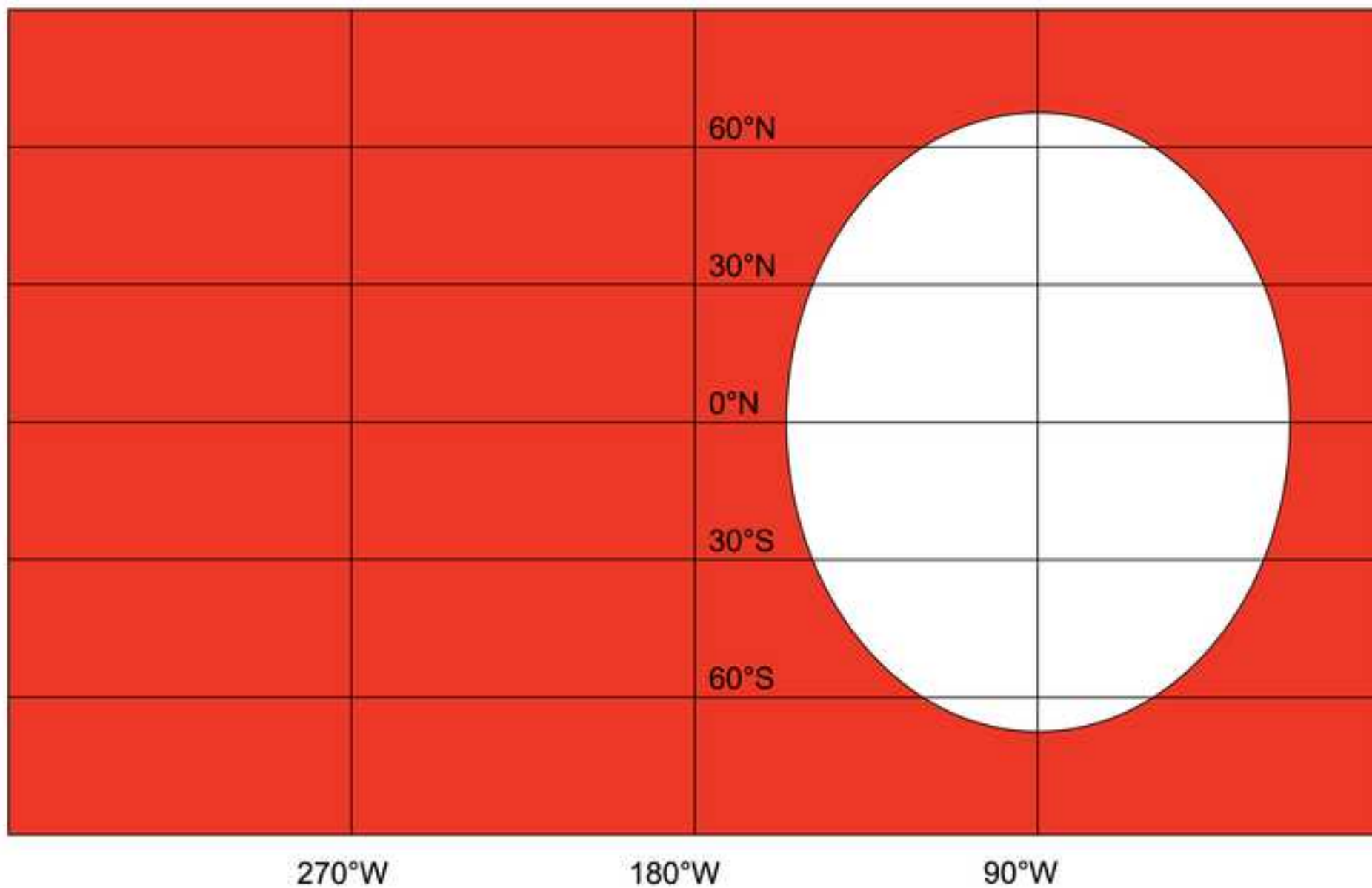


Fig. 8b
[Click here to download high resolution image](#)

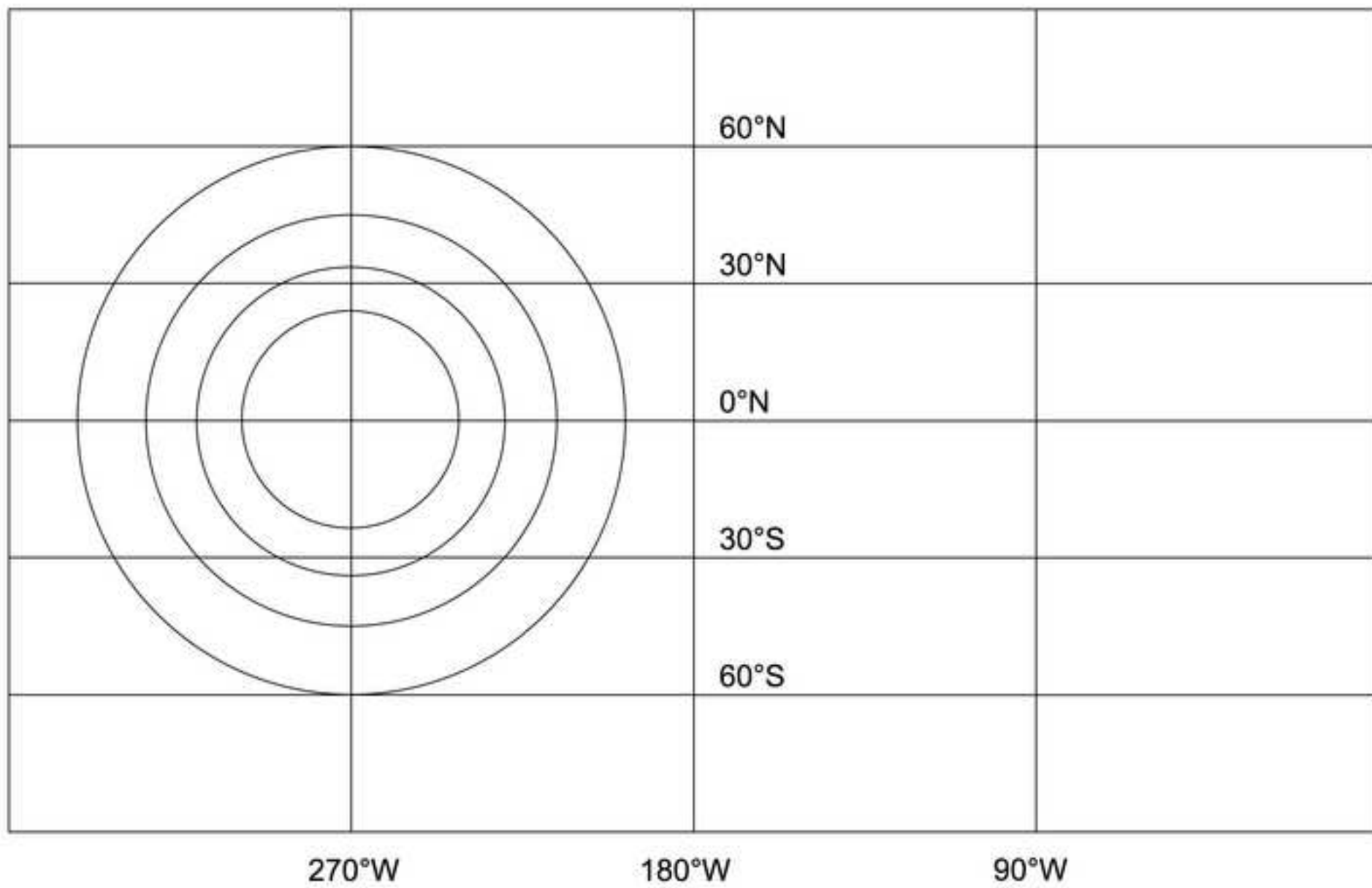


Fig. 8c
[Click here to download high resolution image](#)

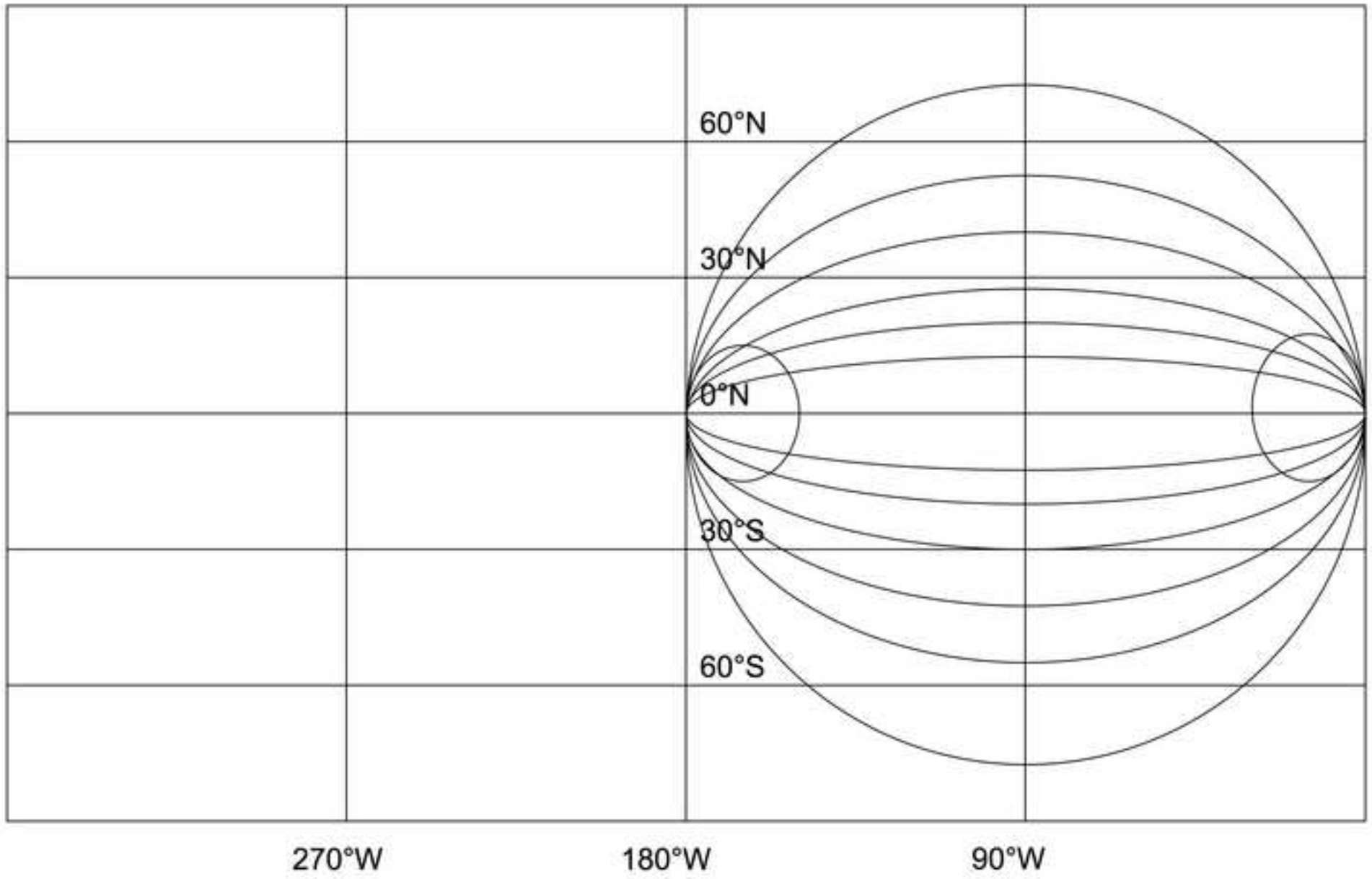


Fig. 8d
[Click here to download high resolution image](#)

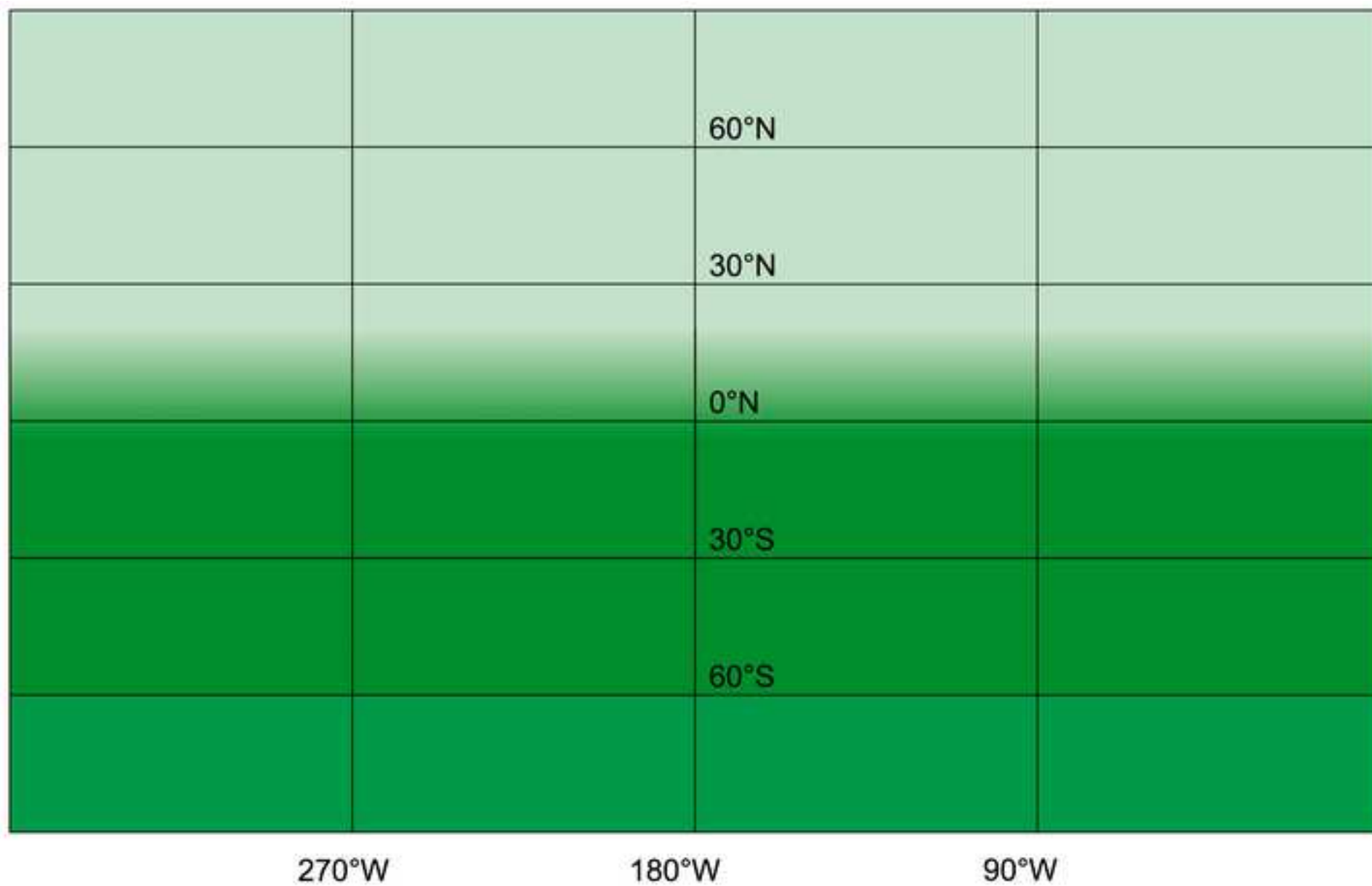


Fig. 8e
[Click here to download high resolution image](#)

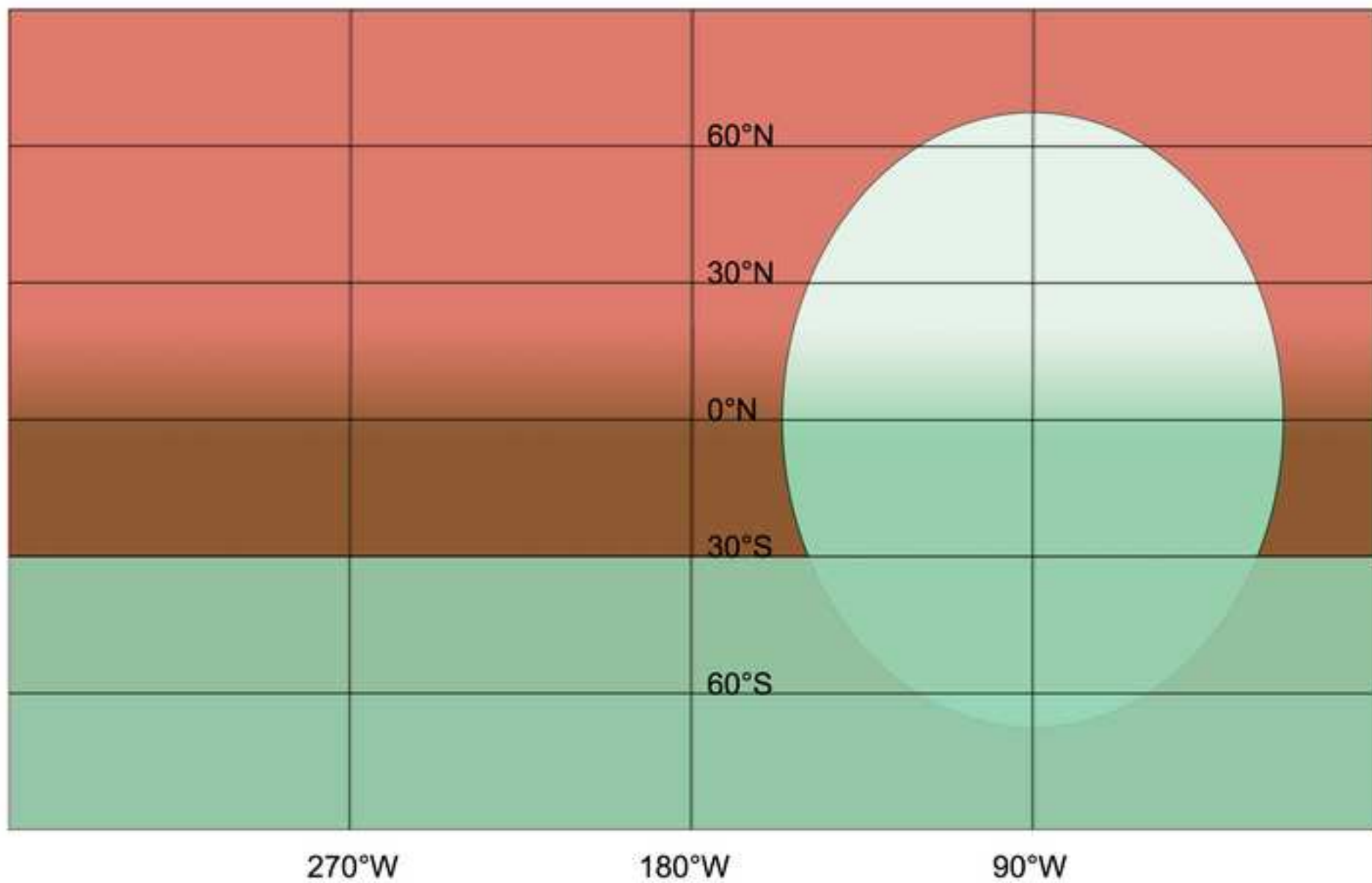


Fig. 8f
[Click here to download high resolution image](#)

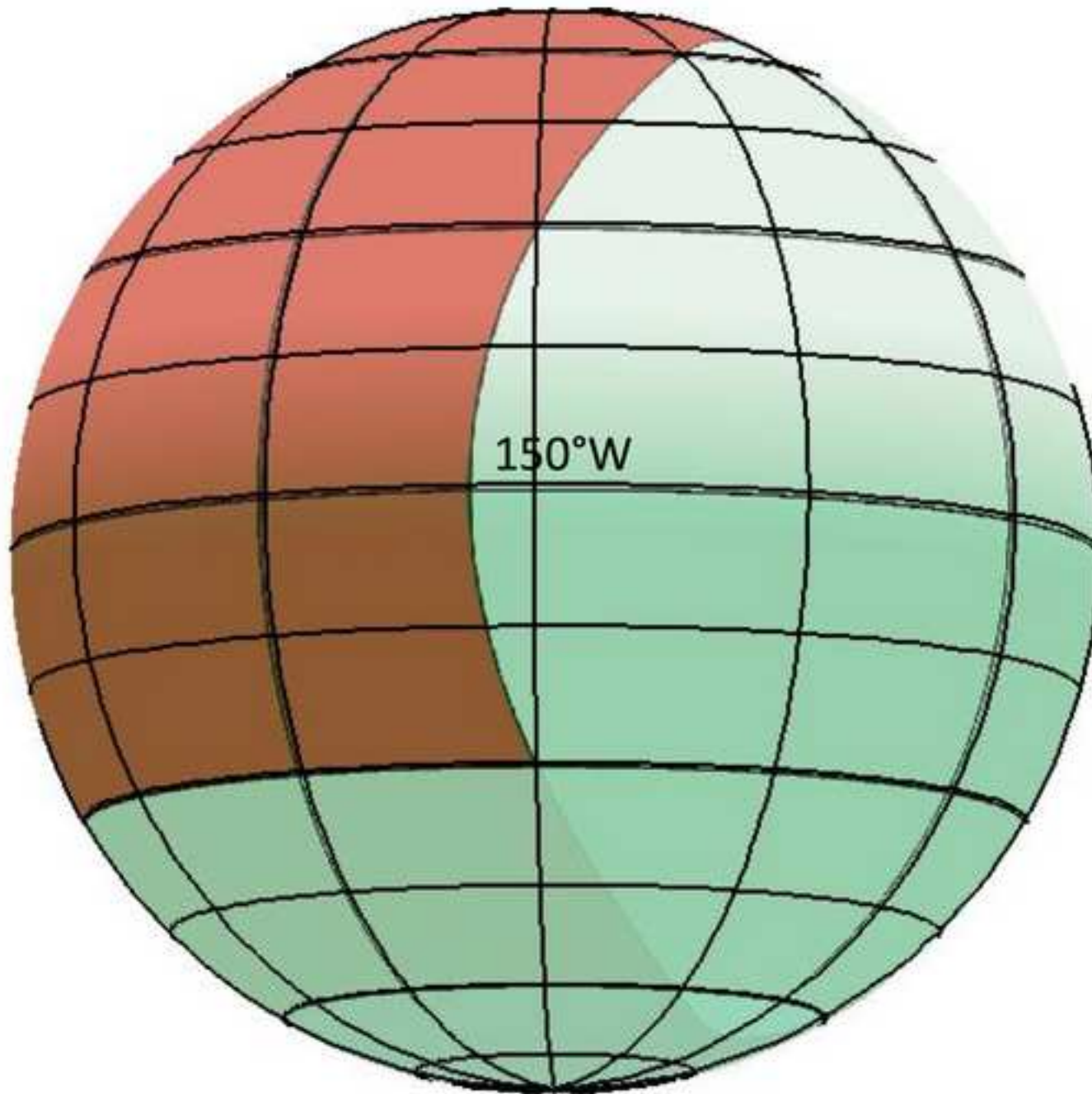


Fig. 8g
[Click here to download high resolution image](#)

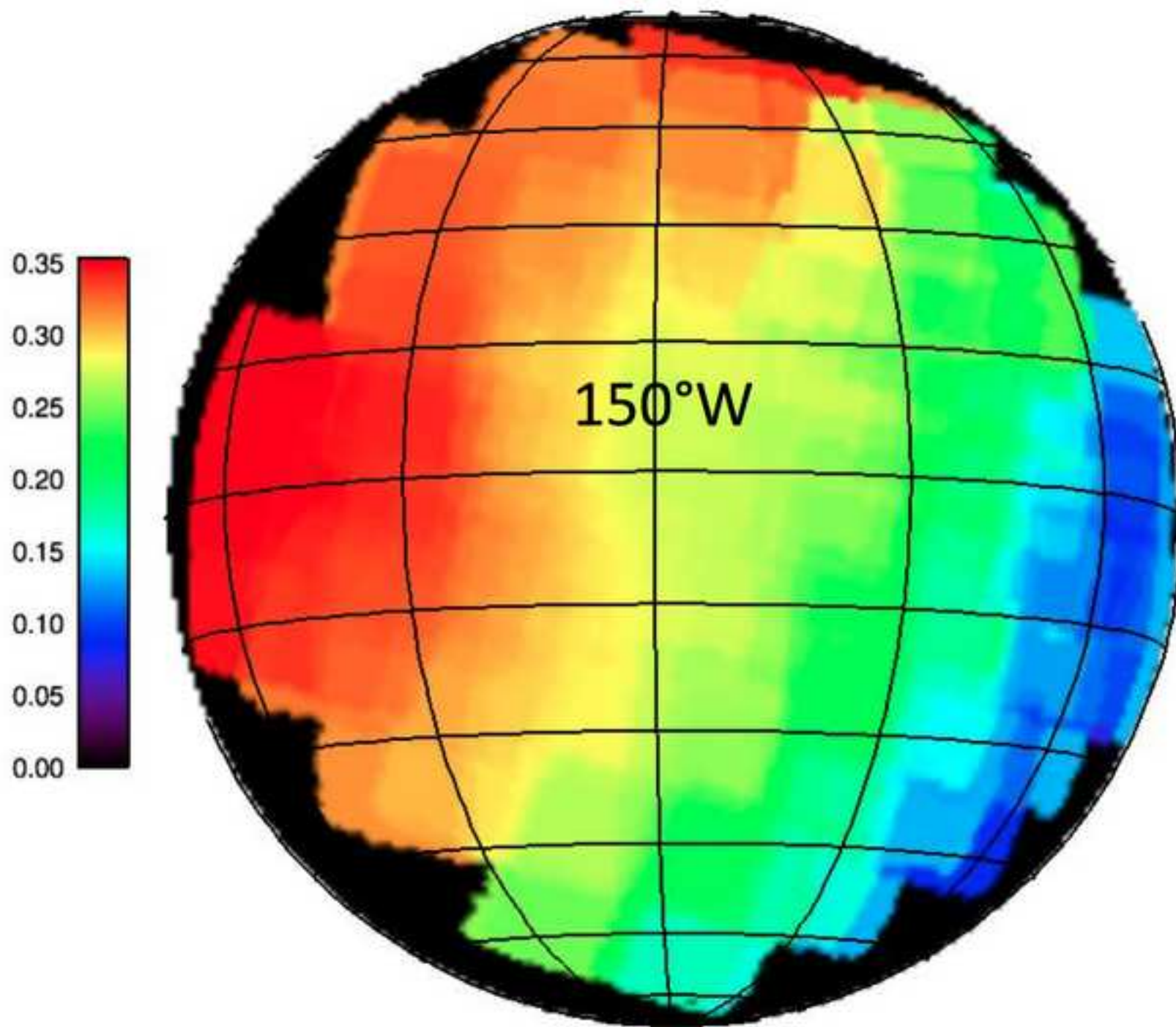


Fig. 9

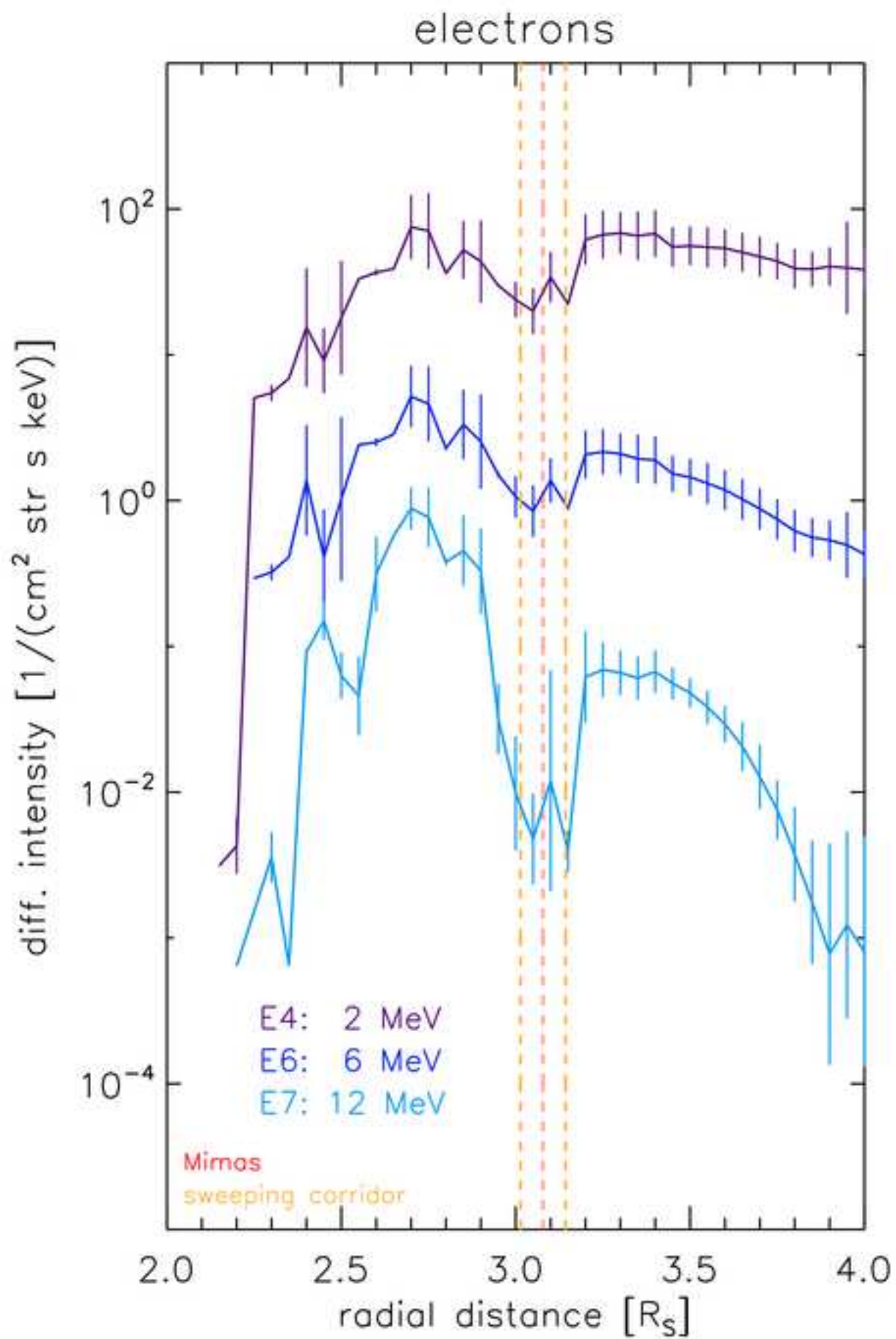
[Click here to download high resolution image](#)

Fig. 10a
[Click here to download high resolution image](#)

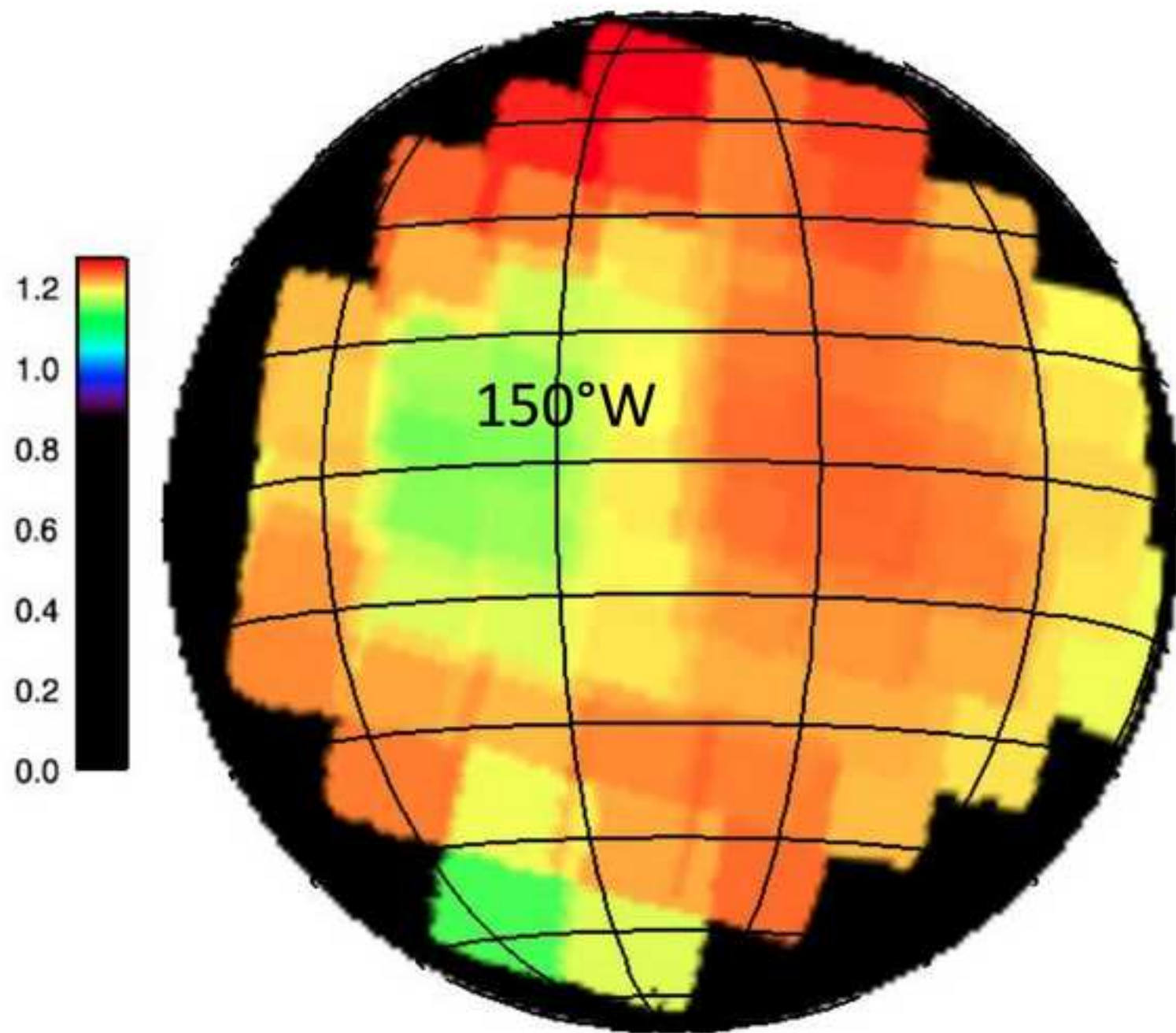


Fig. 10b
[Click here to download high resolution image](#)

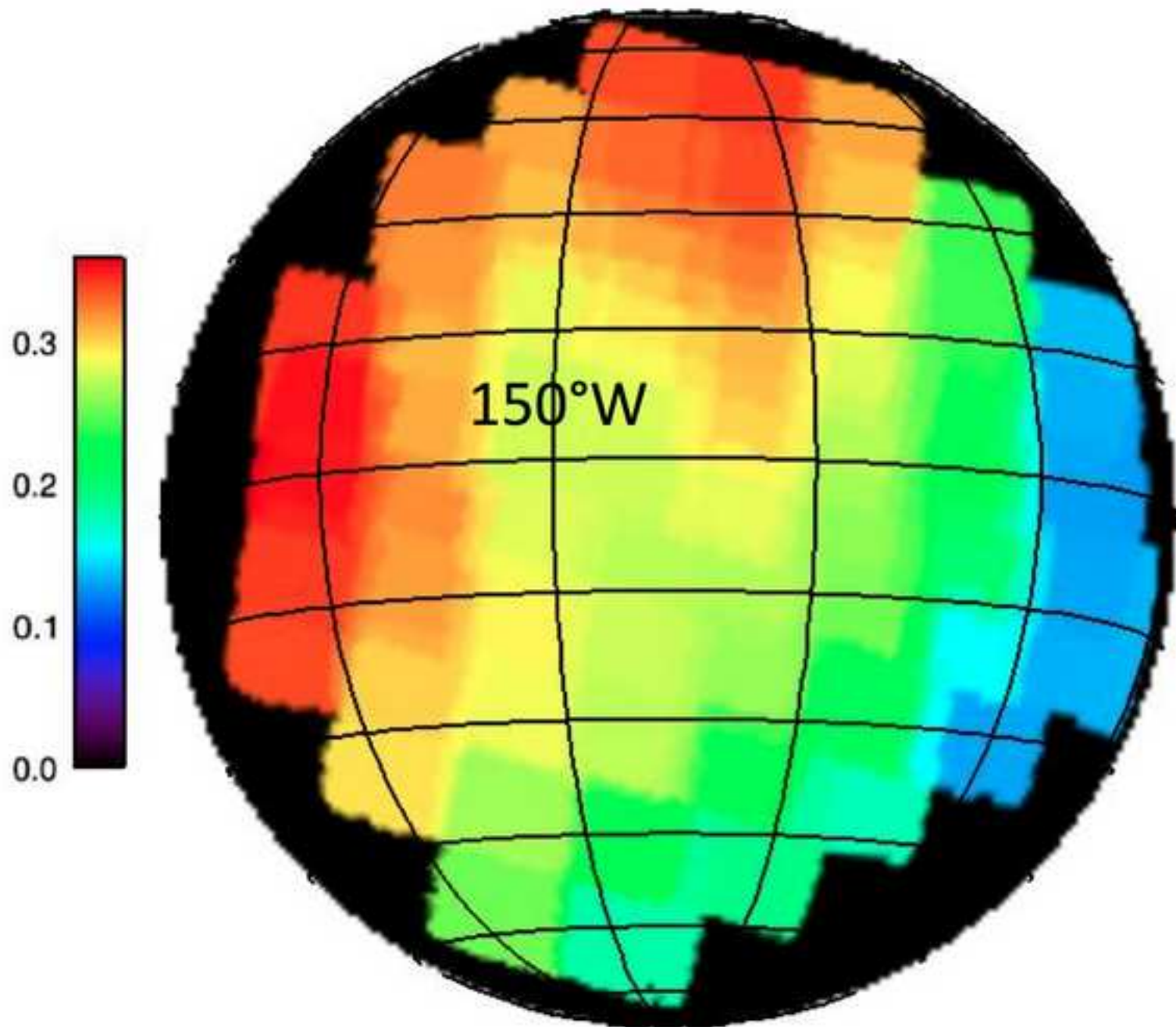


Fig. 11a
[Click here to download high resolution image](#)

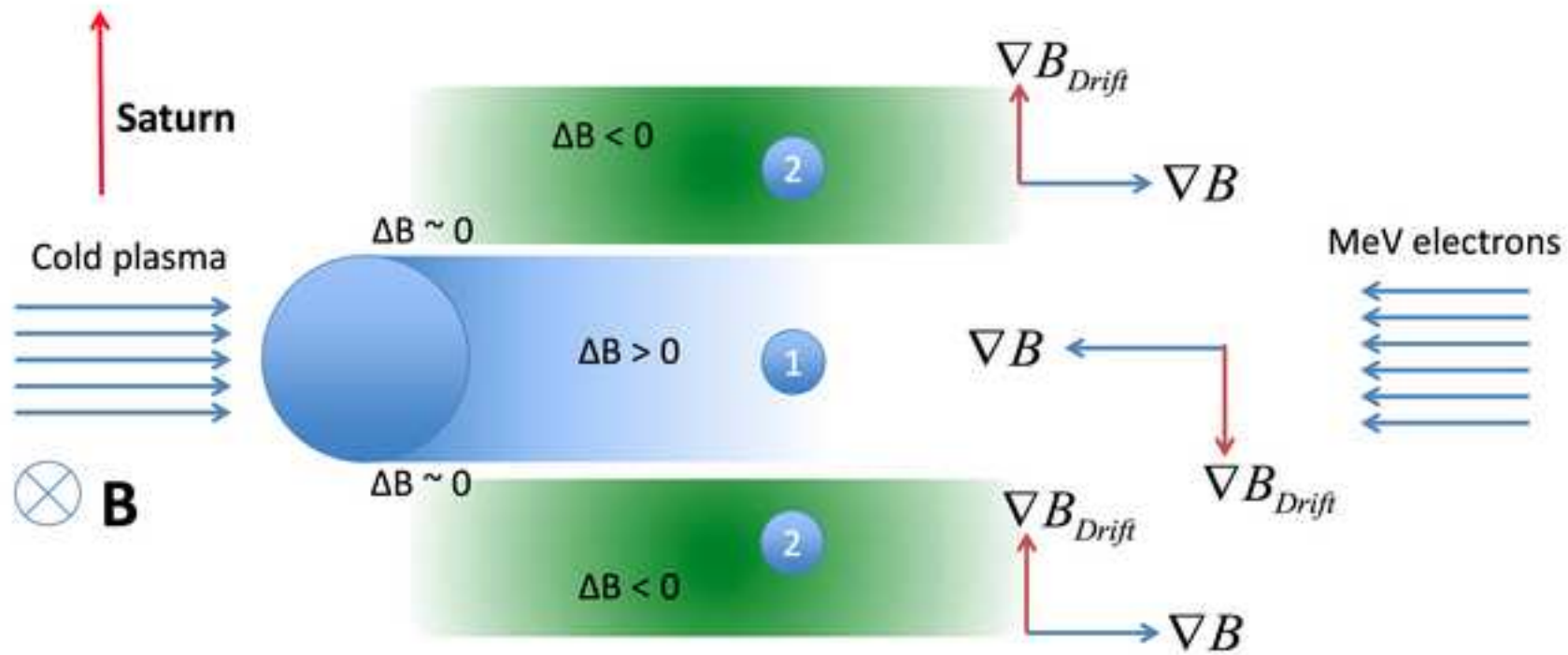


Fig. 11b
[Click here to download high resolution image](#)

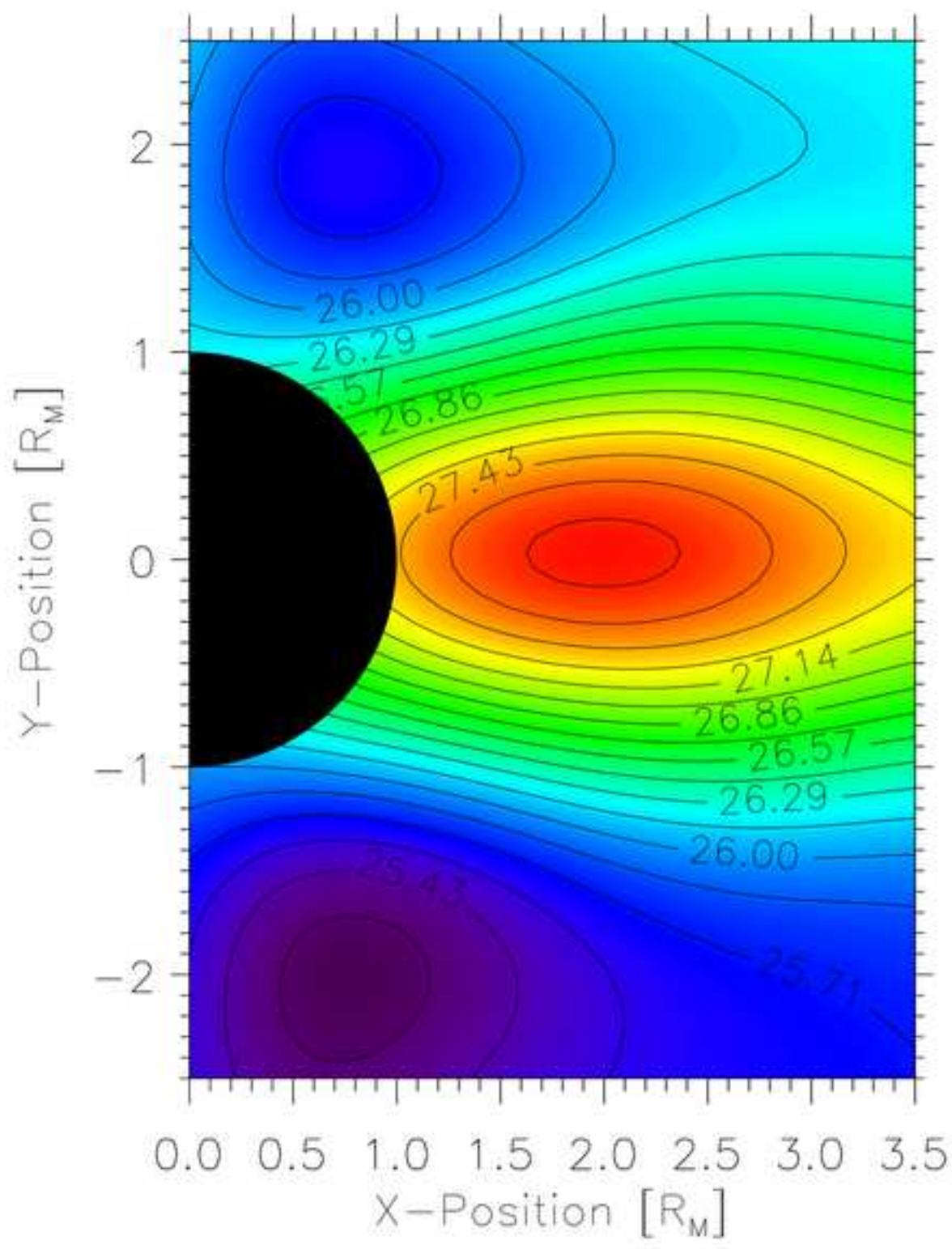


Fig. 12

[Click here to download high resolution image](#)

